INORGANIC CHEMISTRY FRONTIERS

CCS 中国化学会 CHINESE CHEMICAL SOCIETY

ROYAL SOCIETY OF CHEMISTRY

The Balance of Orbital Overlap and Orbital Energy in the Activation of Methane by Actinide Cations: Insights from Inductively Coupled Plasma Tandem Mass Spectrometry

Journal:	*Inorganic Chemistry Frontiers*
Manuscript ID	QI-RES-10-2024-002748.R1
Article Type:	Research Article
Date Submitted by the Author:	27-Nov-2024
Complete List of Authors:	Bubas, Amanda ; Pacific Northwest National Laboratory French, Amanda; Pacific Northwest National Laboratory Melby, Kali; PNNL Rodriguez, Michael; PNNL, Nuclear Chemistry & Engineering Cox, Richard; Pacific Northwest National Laboratory

SCHOLARONE™
Manuscripts

The Balance of Orbital Overlap and Orbital Energy in the Activation of Methane by Actinide Cations: Insights from Inductively Coupled Plasma Tandem Mass Spectrometry

Amanda R. Bubas, Amanda D. French, Kali M. Melby, Michael J. Rodriguez, Richard M Cox*

Pacific Northwest National Laboratory, Richland, WA 99352 USA

ABSTRACT

The actinides present a unique challenge to chemical theory. The classical view of covalent bonding is driven by the extent of spatial overlap of valence orbitals. Modern theory has expanded assessments of covalency to include considerations of orbital energy degeneracy to assess orbital energy mixing between metal and ligand valence orbitals. Actinide-ligand (An- L) bonding has more recently been described as a balance between orbital overlap and orbital energy mixing, where 5f and L valence orbital overlap decreases while energy mixing between An 5f and L valence orbitals increases across the series. To test these existing views, we employed inductively coupled plasma tandem mass spectrometry to examine the kinetic energy dependences of reactions of actinide cations, $Th^+ - Am^+$, with methane. This is the first experimental report of the energy dependences of methane activation reactions involving the cations of Pa, Np, Pu, and Am and the first experimental determination of transuranic $An^+{-}D$, $An^+{-}CD_2$, $An^+{-}CD_3$, and $An^+{-}CD$ bond dissociation energies. The correlation of the measured $An^+{-}CD_2$ bond energies with $E_p(6d^2)$ indicates that An^+ 6d orbitals are the dominant contributors in the $An^+{-}CD_2$ bonds. Close examination of the relative reactivities of An^+ offers additional support that the balance of classical and modern views of molecular bonding may lie between Np^+ and Pu^+ and that the increased reactivity of $Th^+ - Np^+$ may be attributed to the increased spatial extension of the 5f orbitals whereas covalent An^+ bond formation may be more driven by the decreasing energies of the 5f orbitals across the actinide series.

Corresponding Author: *Richard M Cox, Richland, WA 99352. richard.cox@pnnl.gov

INTRODUCTION

Classical theory identifies spatial overlap of molecular orbitals as the critical factor in covalent bonding. Although classical models appear adequate in explaining transition metal chemistry, orbital overlap alone fails to account for the extensive bonding capabilities accessible to the actinides (An). Advanced models used to describe An bonding have expanded to include spin-orbit splitting and electron correlation terms. Recent experimental studies including complementary electronic structure calculations (where spin-orbit contributions and relativistic effects are accounted for) have furthered the discussion of orbital energy degeneracy and orbital energy mixing between metal and ligand valence orbitals leading to covalent bond formation.[1-4] Actinide-ligand (An-L) bonding has recently been described by a balance between orbital overlap and orbital energy mixing.[3, 4] The spatial extension of An 5f orbitals decreases across the series, leading to decreased An-L orbital overlap, whereas the energies of An 5f orbitals also decrease across the series leading to increased mixing in the energies of An 5f and L valence orbitals. Although more recent studies have included discussions of spatial orbital overlap, spin-orbit effects, electron correlation, and orbital energy mixing, current models used to describe An bonding are still incomplete.

Previous studies of fundamental reactions between atomic metal cations and methane have provided a wealth of information related to the physical characteristics (i.e., electronic structure) of the metal reactant that either enable or limit product formation.[5, 6] Studies of methane activation have been expanded to include the actinides, although many of these studies have been limited to Th and U because of radioactivity concerns and difficulties associated with work involving transuranic isotopes. An early ion beam study by Armentrout, Hodges, and Beauchamp examined the reaction of U^+ with perdeuterated methane as a function of ion kinetic energy.[7] The only reaction reported was reaction 1:

$$U^+ + CD_4 \rightarrow UD^+ + CD_3 \qquad (1)$$

The UD^+ cross section increased with increasing energy, which is consistent with expected cross section behavior for an endothermic reaction. Their model of the UD^+ cross section from reaction 1 provided a threshold energy, $E_0 = 1.6 \pm 0.3$ eV, that was used to derive the bond dissociation energy (BDE), $D_0(U^+–D) = 3.0 \pm 0.3$ eV. In a Fourier transform ion cyclotron resonance mass spectrometry (FT-ICR MS) study by Schwarz and co-workers, no reaction was observed between U^+ and methane, which is consistent with the results from Armentrout, Hodges, and Beauchamp because the FT-ICR mass spectrometer can only access thermal energies (nominally 300 K) to observe exothermic and thermoneutral reactions;[8] however, U^+ reacted very efficiently (k/k_{col} = 0.9 – 1.0, where k_{col} is the theoretical rate constant from capture rate theory)[9] with alkenes and cyclopropane. U^+ reacted more efficiently than its lanthanide (Ln) counterpart, Nd^+,[10] and the authors attributed the increased efficiency of the reaction involving U^+ to the involvement of 5f orbitals based on information in a previous review[11] that suggested that the 5f orbitals of the early An^+ can become chemically active because the spatial extents of the 5f, 6d, and 7s orbitals of the early An^+ are similar.

Marçalo et al. employed FT-ICR MS to study the reactions of U^+ and Th^+ with alkanes and alkenes.[12] Although U^+ was unreactive with methane, dehydrogenation of methane by Th^+ was observed, yielding reaction 2:

$$Th^+ + CH_4 \rightarrow ThCH_2^+ + H_2 \qquad (2)$$

Reaction 2 proceeded with an efficiency, $k/k_L = 0.02 \pm 0.01$, where k_L is the Langevin rate constant[13] calculated using the polarizability of methane,[14] 2.448 Å^3. Marçalo et al. hypothesized that other actinides Ac^+, Pa^+, Np^+, and Cm^+ should activate larger hydrocarbons, but activation by Pu^+ and Am^+ should be significantly reduced.[12] This hypothesis was grounded in the availability of two valence non-f electrons in either the ground state or low-lying excited states of An^+, specifically, Ac^+ − Np^+, and Cm^+ have reasonably low-energy excited states (or a ground state) that populate two non-f orbitals.[15] Marçalo et al. suggested that the spatial extension of the 5f

orbitals in the first half of the actinide series would enable the 5f orbitals of the early An^+ to participate in bonding.[12]

Gibson et al. later studied reactions of $Th^+ - Cm^+$ with several alkanes and alkenes at nominally thermal energies (~300 K).[16] The only product they observed in their reactions of $An^+ + CH_4$ was $ThCH_2^+$. Their work provides an assessment of the relative reactivities of these actinides based on the observation (or lack thereof) of product ions resulting from reactions of each An^+ with progressively more reactive hydrocarbons. Specifically, Th^+ is the most reactive actinide, followed by Pa^+, U^+, Np^+, and Cm^+. Pu^+ and Am^+ are the least reactive of the actinides studied, as predicted by Marçalo et al.[12] Gibson et al. considered whether the trend in actinide reactivity is correlated with the promotion energy to a reactive electronic state with a configuration of $5f^{n-2}6d^17s^1$.[16] However, these promotion energies provided a slightly different ordering of reactivities: Th^+ (0.0 eV) ≈ Np^+ (0.0 eV) > U^+ (0.04 eV) > Pa^+ (0.10 eV), than observed, and they concluded that the differences in promotion energies were ultimately too small to account for the observed differences in reactivities. Instead, they attributed the differences in the relative reactivities of the actinides to the degree of 5f orbital participation in C–H and C–C bond activation, where 5f orbital participation is anticipated to be greatest for Pa^+, modest for U^+, and minimal, if any, for Np^+ because the 5f orbitals spatially contract with increasing nuclear size. The reactivities of Pu^+, Am^+, and Cm^+ display a stronger correlation with their promotion energies to $5f^{n-2}6d^17s^1$ configurations, and the authors argued that the 5f orbitals are not active in C–H or C–C bond insertion in these An^+. Notably, their argument is grounded in a classical understanding of bonding and identifies orbital overlap as the primary factor.

Di Santo et al. examined the reactions of Th^{2+} and U^{2+} with methane, ethane, and propane using FTICR-MS and density functional theory (DFT) calculations.[17] The only product observed in the reaction with methane was $ThCH_2^{2+}$. Both Th^{2+} and U^{2+} were reactive towards ethane, yielding $ThC_2H_2^{2+}$ and $UC_2H_4^{2+}$. The DFT calculations revealed that the observed reactions proceed via a bond insertion mechanism, and the calculated energies were consistent with the

promotion energy of An^{2+} to an electronic configuration with two non-f electrons, namely $E_p(6d^2)$ to enable C-H and C-C bond activation.

Marçalo, Santos, and Gibson also examined the reactions of An^{2+} (An = Th – Cm) with several alkanes and alkenes using FTICR-MS (thermal energies, ~300 K).[18] The observed reactions include bond activation and adduct formation to yield doubly charged product ions and electron, hydride, or methide transfer to yield singly charged product ions. The observed reactions proceeded with an efficiency of k/k_{col} ~20 overall (k_{col} is the Su-Chesnavich collisional rate constant[9, 19]). Their discussion of the electron transfer channels to form An^+ is limited to the ordering of the ionization energies of An^+, $IE(An^+)$, where $IE(Cm^+) > IE(Am^+) > IE(Pu^+) > IE(Np^+) \sim IE(U^+) \sim IE(Pa^+) \sim IE(Th^+)$. Their discussion of hydride and methide transfer is limited by a lack of data for the bond dissociation energies of An^+-H and An^+-CH_3. Their discussion of bond activation and adduct formation by An^{2+} focuses on the electronic structures of each An^{2+}. The reactivities of Th^{2+} and Pa^{2+} with hydrocarbons are similar to that of transition metal ions with d^2 or d^3 ground states, the reactivities of Np^{2+} and Cm^{2+} are similar to that of Ln^{2+} ions with one unpaired non-f electron, and the reactivity of U^{2+} lies somewhere between where a d^1 and d^2 or d^3 configuration is crucial to explain its observed reactivity. Pu^{2+} and Am^{2+} have $5f^n$ ground states and high promotion energies to achieve electronic configurations with one or two non-f electrons and do not activate the hydrocarbons included in this study. Further, the authors suggest that Th^{2+} and Pa^{2+} may react by a bond insertion mechanism, Np^{2+} and Cm^{2+} may react by an electrostatic mechanism, and U^{2+} may react by either mechanism. The authors conclude that the $6d^2$ configuration enables bond insertion and accounts for the observed reactivities of Th^{2+}, Pa^{2+}, and U^{2+}, and the 5f electrons are not key contributors to the observed reactivities of Np^{2+}, Pu^{2+}, Am^{2+}, and Cm^{2+}, but may still be involved for Th^{2+} and Pa^{2+}.

Computational studies by de Almeida and Duarte[20, 21] and Di Santo et al.[22] employed density functional theory (DFT) calculations to examine the effects of the electronic structures of several An^+ during methane activation. The calculations by de Almeida and Duarte examined the

initial insertion of An^+ into the methane C-H bond to form the intermediate, $HAnCH_3^+$.[20] Their results identify the number of 5f electrons and promotion energy of An^+ to a reactive state as factors related to An^+ reactivity. Their calculations suggest that an increase in the number of 5f electrons increases the repulsive interactions between An^+ and CH_4, thereby decreasing the kinetic favorability of the An^+ to effectively insert into C–H bonds. Additionally, their calculations loosely support that excitation to a $5f^{n-2}6d^17s^1$ electronic configuration decreases the barrier to C–H bond insertion, thereby increasing reactivity, although FT-ICR MS experiments[16] indicate that promotion to a $6d^17s^1$ electronic configuration does not adequately account for the experimentally observed reactivities. A later computational study by de Almeida and Duarte detailed the reaction mechanism for the activation of methane by Th, Th^+, and Th^{2+} to eliminate H_2.[21] Notably, Th^+ reactivity is similar to that observed for transition metal cations; activation of methane by Th^+ proceeds along multiple spin surfaces, and Th^+–H and Th^+–C bonds primarily involve 6d electrons. The calculations performed by Di Santo et al. examined the potential energy surfaces arising from multiple spin states leading to the formation of $ThCH_2^+$ and UCH_2^+.[22] Their results indicate the presence of a small barrier (0.04 eV) to forming the inserted $HThCH_3^+$ intermediate but conclude that the reaction to form $ThCH_2^+$ is exothermic and proceeds along the doublet surface, and UCH_2^+ formation is endothermic and proceeds along a quartet surface. Notably, none of the three computational studies included spin-orbit contributions, which can be quite large for An^+. Because spin-orbit effects were not included in the calculations, the conclusions do not provide fully quantitative insight into C-H bond activation by An^+.

Cox, Armentrout, and de Jong more recently examined the kinetic energy dependence of the reaction $Th^+ + CH_4$ using Guided Ion Beam Tandem Mass Spectrometry (GIBMS) and observed reaction 2 along with reactions 3 – 5.[23] The collision-induced dissociation (CID) of $[ThCH_4]^+$ with Xe, reaction 6, was also examined.

$$Th^+ + CH_4 \rightarrow ThH^+ + CH_3 \quad (3)$$

$$\rightarrow ThCH_3^+ + H \quad (4)$$

$$\rightarrow \quad ThCH^+ + H + H_2 \qquad (5)$$

$$Th(CH_4)^+ + Xe \quad \rightarrow \quad Th^+ + CH_4 + Xe \qquad (6)$$

Cox, Armentrout, and de Jong observed that while the $ThCH_2^+$ product is present at the lowest, near-thermal energies, the cross section increases with increasing energy, which is inconsistent with reaction 2 being an exothermic, barrierless process, as concluded in previous FT-ICR MS studies. In this study, reaction 2 proceeded with an efficiency $k/k_{col} = 0.002 \pm 0.001$ at the lowest energies studied, where k_{col} is the Su-Chesnavich[9, 19] semi-classical trajectory theoretical rate constant. Reactions 3 – 6 correspond to endothermic processes, and modeling of the cross sections for reactions 2 – 6 provided direct measurements of threshold energies, E_0, used to derive several bond dissociation energies.[23] The potential energy surface (PES) of the $Th^+ + CH_4$ reaction was also investigated using multiple levels of theory and several basis sets. The PES reveals that the barrier observed in the $ThCH_2^+$ cross section corresponds to the barrier of Th^+ insertion into the C–H bond to form the activated HTh^+CH_3 complex, but this barrier is only evident in calculations when spin-orbit contributions are included. This barrier was in part tied to the unique Th^+ J = 3/2 ground level that is a mix between the $^4F_{3/2}$ ($6d^27s$) and $^2D_{3/2}$ ($6d7s^2$) states, where the observed experimental barrier is caused by the increased electron density in the 7s orbital. Consequently, two unpaired 6d electrons promote formation of the activated HTh^+CH_3 complex, and consideration of the mixed character of the Th^+ ground state explains the observed Th^+ reactivity. This argument was further supported by comparison of the transition state barrier height to those observed from Zr^+ ($^4F_{3/2}$, $4d^25s$) and Hf^+ ($^2D_{3/2}$, $5d6s^2$). At similar levels of theory, the barrier for Th^+ falls between the Zr^+ and Hf^+, presumably because the mixed character of Th^+ inhibits bond activation.

Other An studies have established or predicted a low-lying $6d^2$ configuration as an important factor in predicting actinide reactivities and bond dissociation energies.[24-29] Gibson noted that AnO^+ bond formation requires two unpaired 6d electrons on An^+ and established the correlation of AnO^+ BDEs with promotion energies to $6d^2$ electronic configurations, $E_p(6d^2)$.[24]

This analysis was later expanded by Marçalo and Gibson.[25] Other work has extended this correlation to explain the increased reaction efficiency observed for reactions of the actinides with O_2, H_2O, and CO_2.[28, 30] Notably, An^+ with low-lying $6d^2$ electronic configurations display increased reaction efficiencies. The increased reaction efficiencies were further explained by examining the PES for the ground state and reactive state ($6d^2$ configuration) An^+. Specifically, the reaction efficiency is limited by the crossing point (really a crossing seam), C_p, between the potential energy surface evolving from the ground state An^+ reactant and the surface leading to ground state products. This C_p defines the forward rate of the reaction, and barriers are observed when the C_p is not submerged below the reactants' energy. Such barriers were observed for Pu^+ and Am^+ reactions with CO_2.[30]

Although many of the previous studies have offered insight related to actinide bonding and reactivity with a focus on either the spatial extension of 5f orbitals or promotion energies, more recent studies have presented considerable insight into the balance between spatial orbital overlap and An-L orbital energy mixing as factors responsible for actinide reactivity and bonding.[1-4] Kelley et al. presented electronic structure calculations in combination with solution-phase complexation thermodynamic data that reveal that the energies of the 5f orbitals of Am, Cm, Bk, and Cf become progressively lower from Am to Cf.[1] The progressive lowering of An 5f orbitals leads to increased mixing with the molecular orbitals of dipicolinate ligands, thereby increasing the extent of An-L covalency through energy degeneracy between the An and L valence orbitals. A later study by Su et al. includes a combination of relativistic DFT calculations and Cl K-edge X-ray absorption spectroscopy to further illustrate the covalent interactions between An and L driven by energy degeneracy of the An 5f and Cl 3p orbitals in $AnCl_6^{2-}$ (An = Th, U, Np, Pu) complexes.[2] Again, the energies of the An 5f orbitals become progressively lower from Th to Pu, and the extent of orbital mixing between the An 5f orbitals and the Cl 3p orbitals increases, leading to increased covalency across the An series. It is important to note that the degree of orbital energy mixing is dependent upon the ligand under investigation. Murillo et al. presented quantum chemical

calculations to characterize and quantify orbital contributions in actinide-carbene bonds.[4] Their results indicate that orbital overlap and orbital energy mixing increases between U and Np; however, orbital overlap decreases while orbital energy mixing increases between Np and Pu. Accordingly, this study classifies Np as the most covalent actinide.

The present study utilizes an inductively coupled plasma tandem mass spectrometer (ICP-MS/MS) to examine the kinetic energy dependences of the reactions of An^+ (An = Th, Pa, U, Np, Pu, Am) with perdeuterated methane. This is the first experimental report of the energy dependences of methane activation reactions involving Pa, Np, Pu, and Am. The increased energy range afforded by the ICP-MS/MS enables the observation of products resulting from endothermic processes, thereby enabling a direct measurement of product threshold energies used to provide the first experimentally determined values for transuranic bond dissociation energies, $D_0(An^+{-}D)$, $D_0(An^+{-}CD_2)$, $D_0(An^+{-}CD_3)$, and $D_0(An^+{-}CD)$. Strong correlations of the measured $An^+{-}CD_2$ bond energies with An^+ promotion energies to $6d^2$ electronic configurations indicate that An^+ 6d orbitals are the dominant contributors in the resulting $An^+{-}\ CD_2$ bonds. The slope of the correlation of $D_0(An^+{-}D)$ with $E_p(6d)$ appears to be consistent from Th – Pu, although the slope may deviate from the trend, within the experimental uncertainties, for Pu and Am. A closer examination of the relative reactivities of An^+ reveals a reduction in the reactivity of Pu^+ compared to Np^+. Our findings suggest that the balance of orbital overlap and orbital energy lies between Np and Pu, and we anticipate that the spatial extension of An^+ 5f orbitals may have a larger impact on An^+ reactivity whereas orbital energy mixing may be more influential in An^+ bond formation.

METHODS

CAUTION: The actinides used in this work are radioactive. All work was done within the radiological protection controls of specialized laboratories at Pacific Northwest National Laboratory.

Experiments were conducted using an Agilent 8900 ICP-MS/MS located within a radiological facility at Pacific Northwest National Laboratory.[31] This instrument utilizes an

inductively-coupled plasma (ICP) ion source equipped with a quartz double-pass spray chamber and a 100 μL min^{-1} perflouroalkoxy alkane (PFA) nebulizer. The reactant ion beam is mass selected using a quadrupole mass filter (1 amu resolution). The ion beam is directed into an octopole ion guide that is surrounded by the reaction cell where the neutral reactant, CD_4, is introduced. The octopole ion guide is advantageous for its radial trapping capabilities to maximize transmission of precursor and product ions. Precursor and product ions are extracted from the collision reaction cell (CRC) and focused through a second quadrupole mass filter for mass analysis and detection using a standard electron multiplier detector.

Stock multi-element standard solutions containing 1 $ng \cdot g^{-1}$ of Th and U in 2% HNO_3 were prepared. To minimize the quantity of higher activity radioisotopes introduced into the instrument, a multi-element standard solution of 1 $pg \cdot g^{-1}$ of Pa, Np – Am in 2% HNO_3 was also prepared. The isotopes used for each M^+ can be found in Table S1 in the Supporting Information. Perdeuterated methane (CD_4) was used as the neutral reagent. The flow rates of methane ranged from 0.06 - 0.13 mL/min, which correspond to estimated pressures of 2.4 and 4.8 mTorr in the reaction region. Tuning parameters were optimized to provide maximum sensitivity for the high-mass range using the 1 $ng \cdot g^{-1}$ Th and U solutions. The octopole bias was adjusted in intervals from +10 V to -70 V while keeping other cell parameters constant: octopole rf peak-to-peak voltage of 180 V, axial acceleration of 2.0 V, and a kinetic-energy discrimination (KED, the voltage difference between the octopole bias in the CRC and the second quadrupole) of -10.0 V. Data were acquired in triplicate using 1 sec acquisition times per energy per product or reactant ion for the 1 $ng \cdot g^{-1}$ solutions and 4 sec for the 1 $pg \cdot g^{-1}$ solutions.

Absolute reaction cross sections (σ) were calculated from the raw signal intensities using equation 7,[32]

$$I = I_0 e^{-\rho \sigma l} \qquad (7)$$

where I is the intensity of the precursor ion exiting the collision cell, I_0 is the intensity of the precursor ion entering the collision cell, ρ is the number density of the CD_4 neutral reagent in the collision cell, and l is the effective length of the collision cell. I_0 is estimated from the sum of all

ion intensities observed for a given precursor ion selected in the first quadrupole, and l is estimated as the physical length of the collision cell, 10 cm, in the Agilent 8900, although the pressure gradient extends outside of the reaction cell. The uncertainty in l is expected to be ≤ 20% and is included in the absolute uncertainty of the cross section. Individual product ion cross sections (e.g., MD^+) are calculated as percentages of the total reaction cross section calculated in eq. 7. Because the Agilent 8900 operates under multi-collision conditions, the cross sections observed at 2.4 and 4.8 mTorr are extrapolated to zero pressure (i.e., single-collision conditions). Absolute uncertainties in the cross sections are estimated to be ± 50% with relative uncertainties of ± 10%.

The laboratory frame energy is estimated based on the octopole bias using equation 8,[33]

$$E_{Lab} = V_p + \frac{M}{m_{Ar}}\frac{5}{2}k_B T_P - V_{oct} \quad (8)$$

where V_p is the plasma potential (~2 V), M is the mass of the reactant ion, M^+, m_{Ar} is the mass of argon (from the plasma), k_B is Boltzmann's constant, T_p is the ion temperature entering the octopole, and V_{oct} is the octopole bias (negative with respect to ground). In previous work, we conservatively estimated that the temperature of the ions exiting the plasma is 5,000 – 10,000 K, although some collisional cooling is suspected to occur in the differentially pumped region between the ion source and first quadrupole.[28, 30, 31] The average electronic energy for a Boltzmann distribution for temperatures within the 300 – 10,000 K temperature range can be found in Table S1 of the SI. The energy in the center-of-mass (E_{CM}) frame represents the kinetic energy available for a chemical reaction. The relationship between E_{LAB} and E_{CM} is described by equation 9:[32]

$$E_{CM} = E_{LAB} \times m/(m+M) \quad (9)$$

where m is the mass of the neutral reagent, CD_4 = 20 amu, and M is the mass of the metal ion, M^+.

Data Analysis

GIBMS studies have successfully utilized a modified line-of-centers model (mLOC) to determine the BDEs of many ML^+ from kinetic-energy-dependent absolute reaction cross sections.[32, 34] The mLOC model is described by equation 10,[35]

$$\sigma(E) = \sigma_0 \Sigma g_i (E + E_{el} + E_i - E_0)^n/E \quad (10)$$

where σ_0 is an energy-independent scaling factor, E is the relative (E_{CM}) kinetic energy of the reactants, E_{el} is the electronic energy of the metal cation reactant, E_i is the energy of the CD_4 neutral reactant rovibrational states having populations of g_i ($\Sigma g_i = 1$), E_0 is the 0 K reaction threshold, and n is an adjustable parameter that guides the shape of the model.[36] Here, we calculate E_{el} as the average E_{el} from a Boltzmann distribution. Equation 10 was used to model the ICP-MS/MS cross sections found in the data presented below, but it is important to account for the differences between the GIBMS experimental conditions and those in the ICP-MS/MS to successfully model the cross sections from the ICP-MS/MS experiments. GIBMS incorporates a flow tube to collisionally cool ions prior to precursor selection by a magnetic sector mass spectrometer. A conservative estimate of the electronic energy distribution of ions in a GIBMS is 700 ± 400 K.[37-39] Comparisons between GIBMS and ICP-MS/MS cross sections indicate an elevated electronic energy distribution for ions generated in the ICP-MS/MS.[30] The electronic distribution of ions in the ICP-MS/MS is not as extensively characterized as that for GIBMS. As noted above, metal ions are expected to exit the source with temperatures of 5,000 – 10,000 K. At temperatures of 5,000 K and above, the average electronic energy is significant and likely contributes to the observed reactivity; therefore, this must be explicitly accounted for in modeling the cross section. We have adapted equation 10 such that E_{el} is explicitly calculated using a Maxwell-Boltzmann distribution to include temperature of the metal cation source, T_{el}, as an adjustable parameter, along with σ_0, E_0, and n. Equation 10 is fit to each experimental cross section using a non-linear least squares method. Optimized modeling parameters indicate that the temperature of each An^+ is 6,500 ± 1,500 K, though in taking a more conservative approach to providing quantitative thermodynamic information, we include optimized parameters and values based on models over the temperature range of 1,000 K up to 10,000 K. To account for the vibrational and rotational energy of the CD_4 reagent introduced into the collision cell, we assume a temperature of 350 K and estimate the internal rovibrational energy of CD_4 to be 0.09 eV using the Beyer-Swinehart[40] algorithm (a screen capture of the output from CRUNCH[41] is included as Figure S1 in the Supporting Information).

Another notable difference between GIBMS and ICP-MS/MS is that GIBMS operates at extremely low pressures (0.05 – 0.4 mTorr) to promote single collision conditions whereas the ICP-MS/MS operates at higher pressures where the probability of multiple collisions cannot be fully mitigated. The energy from multiple collisions is difficult to account for, resulting in a poorly defined kinetic energy distribution.[32] Our best effort to account for multiple collision conditions involves extrapolation of the ICP-MS/MS cross sections to zero pressure. Previous work suggests that this extrapolation is likely acceptable.[30]

Uncertainties in n and σ_0 are calculated as the standard deviation (1σ) of the acceptable fits. Uncertainty in E_0 is calculated by propagating the standard deviation of the acceptable fits and the standard deviation of the average E_{el}. The exact distribution of E_{el} is not known; however, use of a Maxwell-Boltzmann distribution to calculate E_{el} (where T is allowed to vary but consistently optimizes to $T \approx 6{,}500$ K), and inclusion into equation 10 reproduces the data well. The standard deviation in electronic energy is ≈ 0.25 eV for the lower and upper limits of our temperature estimate (1,000 K and 10,000 K, respectively) and is listed in Table S1. Notably, doppler broadening[32] is not included in the analysis. It is assumed that this falls within the electronic energy distribution that leads to the stated uncertainty.

RESULTS

The absolute cross sections for the reactions of $An^+ + CD_4$ are shown below and correspond to reactions 11 – 15. Note that some of the minor product channels have been multiplied by the indicated factor so that their features are more apparent.

$$An^+ + CD_4 \rightarrow AnD^+ + CD_3 \quad (11)$$

$$\rightarrow AnCD_2^+ + D_2 \quad (12)$$

$$\rightarrow AnCD_3^+ + D \quad (13)$$

$$\rightarrow AnCD^+ + D + D_2 \quad (14)$$

$$\rightarrow \quad AnC^+ + 2\ D_2 \qquad (15)$$

Reactions 11 – 15 are observed for Th^+, Pa^+, and U^+, (Figures 1 – 3, respectively) suggesting that these are the most reactive actinides among those studied here, although the absolute intensity of the reactant ion beam is much higher for the early An^+ (Th^+, Pa^+, and U^+), which provides more sensitivity for observing inefficient reactions, such as reaction 15. Reaction 15 is not observed for Np^+, Pu^+, and Am^+, where the absolute intensity of the reactant ion beam is much smaller (by two orders of magnitude). All product ion cross sections increase with increasing energy, and their energy dependences indicate that reactions 11 – 15 for Th^+, Pa^+, and U^+ proceed via endothermic pathways, or there is a barrier that exceeds the reactants' energies and limits product formation. Reactions 11 – 14 are observed for Np^+ (Figure 4), and the energy dependences of the resulting product ion cross sections are consistent with endothermic reactions. For Th^+, Pa^+, U^+, and Np^+, the initial decline of the $AnCD_2^+$ cross section corresponds to the onset of Reactions 11 and 13. This behavior indicates that there is a shared intermediate between reactions 11 – 13, which is consistent with previous reports of the PESs for the reactions of Th^+ and U^+ with methane.[20-23] The decline in $AnCD_3^+$ coincides with the rise of the $AnCD^+$ cross section and indicates that the $AnCD^+$ product results from the dehydrogenation of the $AnCD_3^+$ product to yield $AnCD^+$ and D_2. For Th^+, Pa^+, and U^+, the rise in the AnC^+ cross section is also associated with the decline of the $AnCD_2^+$ cross section, suggesting that the AnC^+ product likely forms through dehydrogenation of $AnCD_2^+$. The magnitudes of the AnC^+ cross sections indicate that this process is not very favorable. Reaction 15 is no longer observed with Np^+. The reactivities of Pu^+ and Am^+ are significantly decreased compared to the other actinides studied here, and for Pu^+, only reactions 11 and 12 are observed (Figure 5), and for Am^+, only reaction 11 is observed (Figure 6). Again, the product ion cross sections increase with increasing energy, and this energy dependence suggests that the $PuCD_2^+$, PuD^+, and AmD^+ products form endothermically.

All product ion cross sections were modeled using equation 10 to obtain a threshold energy, E_0, and the modeling parameters are listed in Table 1. The AnD^+ cross sections for An = Th, Pa, U, Np, Pu, and Am are presented in Figure 7. The ThD^+ product possesses a threshold of $E_0 = 1.62 \pm 0.81$ eV, PaD^+ possesses a threshold of $E_0 = 1.63 \pm 0.54$ eV, and UD^+ and NpD^+ have thresholds of 1.76 ± 0.71 and 1.70 ± 0.51 eV, respectively. The threshold energies for the AnD^+ products (An = Th – Np) all lie within the same energy range within experimental uncertainties. The threshold energies for PuD^+ and AmD^+ are much higher in energy with $E_0(PuD^+) = 3.31 \pm 0.83$ eV and $E_0(AmD^+) = 3.65 \pm 0.74$ eV.

The $AnCD_2^+$ cross sections for reaction 12 are shown in Figure 8. All $AnCD_2^+$ cross sections increase with increasing energy, which is consistent with the failure of previous FT-ICR MS measurements to observe these reactions at thermal energies.[16] $ThCD_2^+$ is the only product observed at the lowest energy (~0.15 eV), although the $PaCD_2^+$ and $NpCD_2^+$ cross sections possess small exothermic tails, which are likely artifacts of excited states of An^+ that are populated under the conditions of the ICP ion source, as detailed previously.[28, 30] Analysis of the $ThCD_2^+$ cross section observed in the present ICP-MS/MS investigation provides a barrier height of 0.43 ± 0.78 eV. The barrier to $ThCD_2^+$ formation has previously been assessed by GIBMS experiments complimented by CCSD(T) calculations including spin-orbit corrections.[23] The GIBMS study provided a barrier height of 0.28 ± 0.03 eV for perdeuterated methane and attributed the barrier to the mixed $^4F(6d^27s^1)$ and $^2D(6d^17s^2)$ character of the Th^+ ground state. The $PaCD_2^+$ cross section possesses a threshold of $E_0 = 0.59 \pm 0.53$ and is closely followed by the rise in the UCD_2^+ cross section at 0.97 ± 0.68 eV along with the rise in the $NpCD_2^+$ cross section at 0.96 ± 0.47 eV. The $PuCD_2^+$ cross section does not rise until 1.39 ± 0.77 eV, and $AmCD_2^+$ is not observed.

Product ion cross sections resulting from the reactions of Th^+ and U^+ with methane have previously been reported. Armentrout, Hodges, and Beauchamp utilized an early ion beam apparatus to study the reaction of U^+ and perdeuterated methane, reporting only reaction 11.[7] The apparent threshold in the present work is slightly lower in energy than that reported in the early

ion beam study (~1 eV vs. 1.25 eV), Figure 3. The UD^+ cross section observed in the earlier work peaks at ~2 x 10^{-16} cm^2 between 5 and 6 eV whereas the current work shows that the UD^+ cross section peaks at ~6 x 10^{-16} cm^2 at 5 eV. Cox, Armentrout and de Jong utilized GIBMS to study the reaction of Th^+ with methane and observed all processes in the present work except for reaction 15.[23] At the lowest energy reported in Figure 1, 0.1 eV, the cross section is 0.6 x 10^{-16} cm^2 for reaction 12, slightly higher than the 0.2 x 10^{-16} cm^2 observed at ~0.09 eV for the GIBMS work. The cross section corresponding to reaction 12 peaks at 3 x 10^{-16} cm^2, slightly lower than that observed in GIBMS, ≈ 4 x 10^{-16} cm^2. The cross sections for reactions 13 and 14 also peak with similar magnitude to the GIBMS work, albeit with lower apparent thresholds that are consistent with the expected electronic energy distributions of the Th^+ generated in the ICP source. The most notable difference between the processes shown in Figure 1 and those observed in the earlier GIBMS work is reaction 11. The magnitude of the cross section for reaction 11 is near 6.5 x 10^{-16} cm^2 compared to 3.5 x 10^{-16} cm^2 in the GIBMS study. The cause of this difference is not understood but could be related to the differences in operating pressure between the two instruments. Notably, the ICP-MS/MS operates at pressures that are an order of magnitude higher than those used in GIBMS experiments. To compensate, the ICP-MS/MS cross sections have been extrapolated to zero pressure (i.e. rigorous single collision conditions). While this approximation is likely reasonable, as noted by the similarities in the cross sections observed for reactions 12 – 14 shown in Figure 1, it is possible that these cross sections maintain some multi-collisional character that accounts for the difference in magnitude.

DISCUSSION

Assuming no barriers in excess of the endothermicity of reaction, bond dissociation energies for An^+–D, An^+–CD_2, and An^+–CD_3 were derived using the relationship $D_0(M^+– L) = D_0(R–L) – E_0$. These derived bond energies along with bond dissociation energies (BDEs) for An^+–CD^+ and An^+–C are presented in Table 2. To our knowledge, no transuranic BDEs for An^+–D, An^+–CD_2, An^+–CD_3, or An^+–CD have been previously reported, although

An^+−H BDEs have been predicted by Cox, Armentrout, and de Jong.[42] Bond dissociation energies for Th^+−D, Th^+−CD_2, Th^+−CD_3, Th^+−CD, Th^+−C, U^+−D, U^+−CD_2, U^+−CD_3, U^+−CD, and U^+−C have been measured by Armentrout and coworkers.[23, 43-45] These values are included in Table 2 for comparison. The uncertainties included in Table 2 are reflective of the uncertainty of the starting electronic energy distribution of the ICP-MS/MS and potential multicollisional character retained after extrapolation to single collision conditions. We find that our values are comparable to those previously measured by GIBMS experiments, although systematically higher by an average of 0.7 ± 0.5 eV, similar to the uncertainty in the present measurements. Differences in experimental conditions are likely to account for the remaining discrepancies. Still, the uncertainties in our measurements for the Th^+−D, Th^+−CD_2, Th^+−CD_3, Th^+−CD, and U^+−D, U^+−CD_2, U^+−CD_3, and U^+−CD BDEs provide a range for our values that lie within the uncertainties of the analogous GIBMS measurements. The Th^+−C and U^+−C BDEs provided here deviate more noticeably from the analogous GIBMS measurements simply because reaction with CD_4 is an inefficient way to measure An^+−C BDEs, and the magnitude of this cross section is quite small. Experiments utilizing CO as the neutral reactant would enable a more direct determination of the An^+−C BDEs, as was done in the GIBMS experiments.[44, 45] Nevertheless, the BDEs reported here are within reasonable uncertainty of the available GIBMS values for Th^+ and U^+ species and offer confidence in the accuracy of the novel, experimental quantitative information presented for the analogous transuranic species.

A comparison of the measured threshold energies and the relative magnitudes of the cross sections can be used to provide an assessment of the relative reactivities of the actinides with perdeuterated methane. Figures 7 and 8 and Table 1 indicate E_0 for the reaction to form AnD^+ and $AnCD_2^+$ generally increases (i.e. BDEs decrease) across the actinide series. Additionally, the magnitudes of the AnD^+ and $AnCD_2^+$ product cross sections decrease across the series, presumably because formation of these products becomes less thermodynamically favorable moving from Th^+ to Am^+. Our comparison indicates Th^+ is the most reactive actinide and Am^+ is the least reactive

of the actinides studied here. Overall, the order of actinide reactivity with methane appears to be: $Th^+ \geq Pa^+ \geq U^+ \geq Np^+ > Pu^+ > Am^+$, which agrees with the previous ordering of actinide reactivity with hydrocarbons provided by Gibson et al: $Th^+ > Pa^+ > U^+ > Np^+ > Cm^+ > Pu^+ > Am^+$.[16] It is important to note that the assessment of the relative reactivities of the actinides provided by Gibson et al. comes from a systematic FT-ICR MS study where each An^+ was reacted with progressively more reactive hydrocarbons. The relative reactivities were based on the observation of product ions (or lack thereof) at thermal energies. The actinides studied did not react with methane at the thermal energies accessible in an FT-ICR MS, except for the inefficient Th^+ reaction. The information provided by the FT-ICR MS study is reliable; however, the present ICP-MS/MS study provides additional information to the FT-ICR MS studies because of the ability of the ICP-MS/MS to vary the kinetic energy of the reactant ion to examine the energy dependence of the reaction.

Previous studies of the reactions between An^+ and methane have argued that methane activation is limited by the promotion energy of An^+ to an electronic configuration with two unpaired electrons in non-f orbitals.[12] Promotion energies are compiled and listed in Table S2 of the Supporting Information. Gibson et al. previously examined the argument that for An^+ to effectively insert into a C–H bond, the An^+ must be able to access an electronic state with the configuration $5f^{n-2}6d^17s^1$.[16] They concluded that promotion energies to a $5f^{n-2}6d^17s^1$ state for Th^+, Pa^+, U^+, and Np^+ would not accurately reproduce the relative reactivities they observed. The present analysis indicates that the promotion energies of An^+ to a $6d^2$ electronic configuration adequately reproduce the relative reactivities observed in the present ICP-MS/MS study as well as those from the earlier FT-ICR MS experiment. The correlation of $D_0(An^+{-}CD_2)$ provided by the present ICP-MS/MS study with $E_p(6d^2)$ ($r^2 = 0.84$) is shown in Figure 9. The correlation of $D_0(An^+{-}CD_2)$ with $E_p(6d7s)$ ($r^2 = 0.58$) can be found in Figure S2 in the Supporting Information section for comparison. The correlations (r^2 values) for each of the bond dissociation energies with each set of promotion energies are summarized in Table S3 of the Supporting Information. The

correlation of $D_0(An^+{-}CD_2)$ with $E_p(6d^2)$ is stronger than the correlation of $D_0(An^+{-}CD_2)$ with $E_p(6d7s)$; however, the absolute uncertainties of the reported $D_0(An^+{-}CD_2)$ values may impose a confidence limit on the conclusions that can be made from the correlations of bond dissociation energies with promotion energies alone.

The computational study by de Almeida and Duarte identified two factors related to the electronic structure of the An^+ that affect the observed reactivity with methane.[20] They explained that an increase in the number of 5f electrons increased the repulsive interactions between An^+ and CH_4 and, therefore, increased the activation barrier to C–H bond insertion (less kinetically favorable). They also determined that promotion to a $6d^17s^1$ electronic configuration decreased the barrier to C–H bond insertion leading to an increased reactivity. Our results indicate that the correlation of $D_0(An^+{-}CD_2)$ with $E_p(6d7s)$ (Figure S2) is weaker than the correlation of $D_0(An^+{-}CD_2)$ with $E_p(6d^2)$. Work by Marçalo and Gibson has tied $An^+{-}O$ BDEs to $E_p(6d^2)$.[25] The interactions of $An^+{-}L$, where L = O and CH_2, are presumably similar as they both involve formation of two covalent bonds using two unpaired electrons on L. Therefore, it is reasonable that the same promotion energy arguments can be used to explain the interaction of An^+ 6d orbitals in methane activation and $An^+{-}L$ bond formation.

More recently, Cox, Armentrout, and de Jong argued that much like the transition metals, the ability of Th^+ to insert into C–H bonds is limited by the availability of valence orbitals that can accept electrons from the C–H bond being broken.[23] Specifically, the filled 7s orbital of Th^+ (^{2}D, $6d7s^2$) leads to a repulsive interaction whereas Th^+ (^{4}F, $6d^27s$) possesses less electron density along the bond axis thereby reducing the repulsive forces that contribute to the barrier for C–H bond insertion. The authors further detail the enhanced reactivity afforded by the availability of two unpaired d electrons (nd^2 electronic configuration) by comparing the observed $Th^+ + CH_4$ reaction barrier to that of transition metal analogs Zr^+ (^{4}F, $4d^25s$)[46] and Hf^+ (^{2}D, $5d6s^2$)[47] where the barrier to C–H bond insertion is 0.09 eV for Zr^+, 0.30 eV for Hf^+, and 0.19 eV for Th^+ (including spin-orbit corrections). The ability of Th^+ to insert into C–H bonds is attributed to the mixed electronic

ground state of Th^+, where one state possesses two unpaired 6d electrons that are available to accept electron density from the C–H bond breaking. The correlation of E_0 and $D_0(An^+–L)$, (L = CH_2, N, O)[23-25, 27-29] with $E_p(6d^2)$ has been shown to be much stronger than correlations with $E_p(6d^17s^1)$. Our present results offer additional support for the requirement of An^+ to access a $6d^2$ configuration to effectively form chemical bonds by examining the correlation of BDEs of $An^+–CD_2$ to $E_p(6d^2)$. Figure 9 suggests An^+ 6d orbitals are the primary contributors in $An^+–CD_2$ bond formation.

Notably, the above analysis has assumed a covalent interaction between An^+ and L. This is unlikely to be fully accurate. Armentrout recently proposed a model to explain LnO^+ BDEs as correlated to Ln^{2+} (5d) + O^-.[34] This model, which exhibits a slope of unity, shows a better correlation than $D_0(Ln^+–O)$ vs. $E_p(5d^2)$. It is possible that a similar model offers a more quantitative explanation of the bonding interactions between An^+ and CH_2. The correlation of $D_0(An^+–CD_2)$ with this model is presented in Figure S3 in the SI. The correlation ($r^2 = 0.74$) is reasonably similar to that found in Figure 9, and certainly within experimental uncertainty. Nevertheless, whether the bond is covalent, ionic, or polar covalent, the same orbitals appear to be involved.

To account for the observed reactivity of An^+ with methane, Gibson et al. revised their promotion energy argument by adding that the relative reactivities of the early actinides are affected by the degree of 5f orbital participation in bond activation, with 5f orbital participation expected to be the highest for Pa^+, modest for U^+, and minimal for Np^+.[16] The 5f orbitals of Pu^+, Am^+, and Cm^+ were not anticipated to be active in C–H or C–C bond insertion; therefore, promotion energy arguments, i.e. $E_p(6d7s)$, were satisfactory in explaining the observed reactivities of the later actinides. Their argument was built based on the earlier observation[12] that the spatial extension of the 5f orbitals is larger for the early An^+ and is progressively smaller with increasing nuclear size; thus, the early An can utilize the 5f orbitals to insert into C–H bonds. Their

reasoning may qualitatively explain the observed An^+ reactivity but is grounded in a classical view of the relationship between orbital overlap and bonding.

Previous investigations of AnN^+ and AnO^+ have argued that a dual analysis may be important to adequately describe bonding in the actinides. An analysis of the correlation of AnN^+ BDEs determined from the reactions of $An^+ + NO$ ($An^+ = Th^+, U^+ - Am^+$) with promotion energies to a $6d^2$ configuration offers evidence to support the argument for a dual analysis.[48] A close examination of the trend[25] of $An^+{-}O$ BDEs vs. $E_p(6d^2)$ also suggests that a deviation from the trend may occur between Pu^+ and Am^+. A deviation in the trend suggests that other factors, presumably the 5f orbitals, may become more important in forming $An^+{-}L$ bonds. The correlation of the BDEs of $An^+{-}D$ from the present ICP-MS/MS experiment to $E_p(6d)$ is shown in Figure 10. The BDEs for $An^+{-}D$ show a strong correlation ($r^2 = 0.96$) with $E_p(6d)$. (The correlation of $D_0(An^+{-}D)$ using values from GIBMS studies of the reactions of Th^+ and U^+ with D_2[42, 43] and values from the present ICP-MS/MS study for Pa, Np, Pu, and Am can be found in Figure S4 of the Supporting Information). The slope of the correlation for Th – Am is m = -1.2, but a deviation in slope may exist starting at Pu^+. If the trend line is broken into two trends, the slope of the trend line for Th – Np is m = -1.5, and the slope of the correlation from Pu to Am is m = -0.5. A shift in slope may indicate the presence of a shift in the orbitals involved in forming $An^+{-}D$ bonds between Np and Pu, though more work is needed to further the discussion and validation of a two-component analysis. The promotion energy of An^+ to an electronic configuration with two unpaired electrons in non-f orbitals has been identified as a limiting factor in the ability of An^+ to effectively insert into C–H bonds.[12] It is important to note that AnD^+ formation may not exclusively proceed via a mechanism that includes bond insertion to form $[D_3C\text{-}An\text{-}D]^+$, but rather AnD^+ formation may also reasonably occur via a mechanism that involves an $An^+{---}D{-}CD_3$ complex, enabling direct abstraction of D from CD_4. A similar mechanism has been suggested by Bubas, Owen, and Armentrout to rationalize the inefficient formation of ThF^+ and UF^+ by reactions of Th^+ and U^+ with CF_4.[49] A direct abstraction of D to form AnD^+ would not necessarily be limited by promotion

energy to a 6d electronic configuration but would rather require precise alignment of the reactants posing instead a kinetic barrier rather than an energetic barrier to reaction. In a direct abstraction mechanism, the d or f orbitals could reasonably be involved. Previous studies have indicated that the 5f orbitals become progressively lower in energy for the later An, such that the 5f orbitals lie even lower in energy than the 6d orbitals.[1, 2, 4] Notably, no such trend can be ascertained from Figure 9 because $AmCD_2^+$ is not observed. A single model that properly accounts for several complex factors that contribute to actinide bond formation remains elusive; therefore, two models may be needed to provide a more effective and accurate description of bonding across the actinide series. Notably, a two-model approach may fit with the data in Figure 10, but additional work with the later An^+ (i.e. Bk^+ and on) is required to distinguish whether a second model is necessary to explain bonding in the late actinides.

It is also important to note that the orbitals involved in bond activation may not be the same as the orbitals involved in bonding in the final product. The previous FT-ICR MS work[16-18] with hydrocarbons has established the requirement of two unpaired non-f electrons to activate the C-H bond and form an inserted intermediate, $H\text{-}An^+\text{-}C_xH_y$. Our analysis indicates that $E_p(6d^2)$ explains the observed reactivity; thus, two 6d electrons are likely critical to form the inserted intermediate. Notably, this analysis does not exclude 5f participation; it only indicates that the 6d electrons are important to the bond activation. Presumably, as the lowest energy product observed (except for Am^+), E_0 for $AnCD_2^+$ in the current work also reflects the importance of the 6d electrons in bond activation. Nevertheless, bond dissociation energies are independent of the reaction used to determine them. In this work, we compare AnD^+ BDEs determined by ICP-MS/MS to those determined by GIBMS for ThD^+ and UD^+ from reactions with D_2.[42, 43] The correlations in Figures 9 and 10 are independent of the bond activation event and do not necessarily give insight into the bond activation leading to the product formation. The correlations in Figures 9 and 10 only give insight into the orbitals involved in the formation of that bond.

Electronic structure calculations (complementary to solution phase thermodynamic data) presented by Kelley et al. reveal that the energies of the 5f orbitals decrease from Am, Cm, Bk, to Cf.[1] This decrease enables energetic mixing with the molecular orbitals of the ligands they investigated, resulting in increased An-L covalency. Similar conclusions were made by Su et al. in their investigation of $AnCl_6^{2-}$ (An = Th, U, Np, Pu) complexes.[2] Their relativistic DFT calculations indicated that the energies of the An 5f orbitals decreased from Th to Pu, such that the energies of Pu's 5f orbitals were nearly degenerate with those of the Cl 3p orbitals. This degeneracy leads to increased energy mixing between the An 5f and Cl 3p orbitals, leading to an increase in covalency across the An series; however, the degree of orbital mixing, and therefore extent of covalent character, is heavily influenced by the ligand under investigation. Quantum chemical calculations by Murillo et al. indicate that from U to Np, orbital overlap and orbital energy mixing increases, although from Np to Pu, orbital overlap decreases while orbital energy mixing increases.[4] The correlation of $D_0(An^+–D)$ with $E_p(6d)$ and the possible change in slope that occurs between Np and Pu may offer direct evidence that the bonding in the later actinides, beginning with Pu, may involve increased participation of the 5f orbitals and decreased contributions from the 6d orbitals.

CONCLUSIONS

Based on strong correlations of $D_0(An^+–CD_2)$ with $E_p(6d^2)$, the 6d orbitals are the primary contributors to $An^+–CD_2$ bond formation. The correlation of $D_0(An^+–D)$ with $E_p(6d)$ is clear, though a shift in slope may occur between Np and Pu. A change in slope in the correlation of bond dissociation energies and promotion energies to a 6d electronic configuration may suggest that 6d orbitals are the primary contributors to bonding for Th – Np whereas other orbitals, presumably the 5f orbitals, may become the dominant contributors to bonding for the later An^+. We anticipate that increased spatial extension of the 5f orbitals contributes to the increased reactivity observed for the early An^+, although bond formation involving the 5f orbitals is likely to be driven by factors related to the energies of the 5f orbitals and becomes more relevant for the later An^+. Our work

also indicates that the shift from classical orbital overlap arguments to more recent energy degeneracy arguments occur between Np and Pu based on the significant reduction in Pu^+ reactivity compared to Np^+. An^+ chemistry appears to be governed by a balance between orbital overlap and orbital energetics, where an increase in An^+ reactivity can be attributed to the increased spatial extension of the 5f orbitals for the early An^+, and increased participation of the 5f orbitals in An^+ bond formation can be attributed to the decreasing energies of the 5f orbitals in the later An^+.

ACKNOWLEDGEMENT

This research was supported by the Open Call Initiative under the Laboratory Directed Research and Development (LDRD) Program at Pacific Northwest National Laboratory (PNNL). PNNL is a multi-program national laboratory operated for the U.S. Department of Energy (DOE) by Battelle Memorial Institute under Contract No. DE-AC05-76RL01830.

REFERENCES

1. Kelley, M. P.; Su, J.; Urban, M.; Luckey, M.; Batista, E. R.; Yang, P.; Shafer, J. C., On the origin of covalent bonding in heavy actinides. *Journal of the American Chemical Society* **2017,** *139* (29), 9901-9908.
2. Su, J.; Batista, E. R.; Boland, K. S.; Bone, S. E.; Bradley, J. A.; Cary, S. K.; Clark, D. L.; Conradson, S. D.; Ditter, A. S.; Kaltsoyannis, N.; Keith, J. M.; Kerridge, A.; Kozimor, S. A.; Löble, M. W.; Martin, R. L.; Minasian, S. G.; Mocko, V.; La Pierre, H. S.; Seidler, G. T.; Shuh, D. K.; Wilkerson, M. P.; Wolfsberg, L. E.; Yang, P., Energy-Degeneracy-Driven Covalency in Actinide Bonding. *Journal of the American Chemical Society* **2018,** *140* (51), 17977-17984.
3. Pace, K. A.; Klepov, V. V.; Berseneva, A. A.; Zur Loye, H. C., Covalency in actinide compounds. *Chemistry–A European Journal* **2021,** *27* (19), 5835-5841.
4. Murillo, J.; Seed, J. A.; Wooles, A. J.; Oakley, M. S.; Goodwin, C. A.; Gregson, M.; Dan, D.; Chilton, N. F.; Gaunt, A. J.; Kozimor, S. A., Carbene complexes of plutonium: structure, bonding, and divergent reactivity to lanthanide analogs. *Journal of the American Chemical Society* **2024,** *146* (6), 4098-4111.
5. Shayesteh, A.; Lavrov, V. V.; Koyanagi, G. K.; Bohme, D. K., Reactions of atomic cations with methane: gas phase room-temperature kinetics and periodicities in reactivity. *The Journal of Physical Chemistry A* **2009,** *113* (19), 5602-5611.
6. Armentrout, P. B., Methane Activation by 5 d Transition Metals: Energetics, Mechanisms, and Periodic Trends. *Chemistry–A European Journal* **2017,** *23* (1), 10-18.
7. Armentrout, P. B.; Hodges, R. V.; Beauchamp, J. L., Endothermic Reactions of Uranium Ions with N_2, D_2, and CD_4. *J. Chem. Phys.* **1977,** *66* (10), 4683.

8. Heinemann, C.; Cornehl, H. H.; Schwarz, H., Hydrocarbon activation by "bare" uranium cations: formation of a cationic uranium-benzene complex from three ethylene units. *Journal of organometallic chemistry* **1995,** *501* (1-2), 201-209.
9. Su, T.; Chesnavich, W. J., Parametrization of the ion–polar molecule collision rate constant by trajectory calculations. *The Journal of Chemical Physics* **1982,** *76* (10), 5183-5185.
10. Cornehl, H. H.; Heinemann, C.; Schroeder, D.; Schwarz, H., Gas-phase reactivity of lanthanide cations with hydrocarbons. *Organometallics* **1995,** *14* (2), 992-999.
11. Pepper, M.; Bursten, B. E., The electronic structure of actinide-containing molecules: a challenge to applied quantum chemistry. *Chemical Reviews* **1991,** *91* (5), 719-741.
12. Marçalo, J.; Leal, J. P.; de Matos, A. P., Gas Phase Actinide Ion Chemistry: Activation of Alkanes and Alkenes by Thorium Cations. *Int. J. of Mass Spectrom. Ion Proc.* **1996,** *157-158*, 265-274.
13. Langevin, M. In *Une formule fondamentale de théorie cinétique*, Annales de chimie et de physique, Series, 1905; pp 245-288.
14. Johnson III, R. D. NIST Computational Chemistry Comparison and Benchmark Database. http://cccbdb.nist.gov/ (accessed April 12, 2018).
15. Kramida, A.; Ralchenko, Y.; Reader, J., NIST atomic spectra database. *NIST standard reference database* **2018,** *78*.
16. Gibson, J. K.; Haire, R. G.; Marçalo, J.; Santos, M.; Pires de Matos, A.; Mrozik, M. K.; Pitzer, R. M.; Bursten, B. E., Gas-Phase Reactions of Hydrocarbons with An^+ and AnO^+ (An = Th, Pa, U, Np, Pu, Am, Cm): The Active Role of 5f Electrons in Organoprotactinium Chemistry. *Organometallics* **2007,** *26* (16), 3947-3956.
17. Di Santo, E.; Santos, M.; Michelini, M. C.; Marçalo, J.; Russo, N.; Gibson, J. K., Gas-phase reactions of the bare Th2+ and U2+ ions with small alkanes, CH4, C2H6, and C3H8: experimental and theoretical study of elementary organoactinide chemistry. *Journal of the American Chemical Society* **2011,** *133* (6), 1955-1970.
18. Marcalo, J.; Santos, M.; Gibson, J. K., Gas-phase reactions of doubly charged actinide cations with alkanes and alkenes-probing the chemical activity of 5f electrons from Th to Cm. *Phys. Chem. Chem. Phys.* **2011,** *13* (41), 18322-18329.
19. Su, T., Parametrization of kinetic energy dependences of ion–polar molecule collision rate constants by trajectory calculations. *The Journal of chemical physics* **1994,** *100* (6), 4703-4703.
20. De Almeida, K.; Duarte, H., Gas-phase methane activation by the Ac+− Pu+ Ions: Theoretical insights into the role of 5f electrons/orbitals in early actinide chemistry. *Organometallics* **2009,** *28* (11), 3203-3211.
21. de Almeida, K. J.; Duarte, H. A., Dehydrogenation of Methane by Gas-Phase Th, Th^+, and Th^{2+}: Theoretical Insights into Actinide Chemistry. *Organometallics* **2010,** *29*, 3735-3745.
22. di Santo, E.; Michelini, M. d. C.; Russo, N., Methane C-H Bond Activation by Gas-Phase Th^+ and U^+: Reaction Mechanisms and Bonding Analysis. *Organometallics* **2009,** *28* (13), 3716-3726.
23. Cox, R. M.; Armentrout, P. B.; de Jong, W. A., Activation of CH_4 by Th^+ as Studied by Guided Ion Beam Mass Spectrometry and Quantum Chemistry. *Inorg. Chem.* **2015,** *54* (7), 3584-3599.
24. Gibson, J. K., Role of Atomic Electronics in f-Element Bond Formation: Bond Energies of Lanthanide and Actinide Oxide Molecules. *J. Phys. Chem. A* **2003,** *107*, 7891-7899.
25. Marçalo, J.; Gibson, J. K., Gas-Phase Energetics of Actinide Oxides: An Assessment of Neutral and Cationic Monoxides and Dioxides from Thorium to Curium. *J. Phys. Chem. A* **2009,** *113* (45), 12599-12606.
26. Pereira, C. C. L.; Marsden, C. J.; Marçalo, J.; Gibson, J. K., Actinide Sulfides in the Gas Phase: Experimental and Theoretical Studies of the Thermochemistry of AnS (An = Ac, Th, Pa, U, Np, Pu, Am and Cm). *Phys. Chem. Chem. Phys.* **2011,** *13* (28), 12940-12958.

27. Cox, R. M.; Kafle, A.; Armentrout, P. B.; Peterson, K. A., Bond Energy of ThN^+: A Guided Ion Beam and Quantum Chemical Investigation of the Reactions of Thorium Cation with N_2 and NO. *J. Chem. Phys.* **2019,** *151* (3), 034304.
28. Cox, R. M.; Harouaka, K.; Citir, M.; Armentrout, P. B., Activation of CO_2 by Actinide Cations (Th^+, U^+, Pu^+, and Am^+) as Studied by Guided Ion Beam and Triple Quadrupole Mass Spectrometry. *Inorg. Chem.* **2022**, 8168-8181.
29. Bubas, A. R.; Kafle, A.; Stevenson, B. C.; Armentrout, P. B., The Bond Energy of UN^+: Guided Ion Beam Studies of the Reactions of U^+ with N2 and NO. *J. Chem. Phys.* **2024,** *160*, 164305.
30. Cox, R. M.; Melby, K. M.; French, A. D.; Rodriguez, M. J., f-Block Reactions of Metal Cations with Carbon Dioxide Studied by Inductively Coupled Plasma Tandem Mass Spectrometry. *Phys. Chem. Chem. Phys.* **2024**.
31. Harouaka, K.; Allen, C.; Bylaska, E.; Cox, R. M.; Eiden, G. C.; Vacri, M. L. d.; Hoppe, E. W.; Arnquist, I. J., Gas-Phase Ion-Molecule Interactions in a Collision Reaction Cell with Triple Quadrupole-Inductively Coupled Plasma Mass Spectrometry: Investigations with N_2O as the Reaction Gas. *Spectrochim. Acta Part B At. Spectrosc.* **2021,** *186*, 106309.
32. Armentrout, P. B., Mass Spectrometry - Not Just a Structural Tool: The Use of Guided Ion Beam Tandem Mass Spectrometry to Determine Thermochemistry. *J. Am. Soc. Mass Spectrom.* **2002,** *13* (5), 419-434.
33. Yamada, N., Kinetic Energy Discrimination in Collision/Reaction Cell ICP-MS: Theoretical Review of Principles and Limitations. *Spectrochim. Acta Part B At. Spectrosc.* **2015,** *110*, 31-44.
34. Armentrout, P. B., Periodic Trends in Gas-Phase Oxidation and Hydrogenation Reactions of Lanthanides and 5d Transition Metal Cations. *Mass Spectrom. Rev.* **2022,** (41), 606-626.
35. Armentrout, P. B., The Kinetic Energy Dependence of Ion-Molecule Reactions: Guided Ion Beams and Threshold Measurements. *Int. J. Mass Spectrom.* **2000,** *200*, 219-241.
36. Muntean, F.; Armentrout, P. B., Guided Ion Beam Study of Collision-Induced Dissociation Dynamics: Integral and Differential Cross Sections. *J. Chem. Phys.* **2001,** *115*, 1213-1228.
37. Sievers, M. R.; Chen, Y.-M.; Elkind, J. L.; Armentrout, P. B., Reactions of Y^+, Zr^+, Nb^+, and Mo^+ with H_2, HD, and D_2. *J. Phys. Chem.* **1996,** *100*, 54-62.
38. Haynes, C. L.; Armentrout, P. B., Thermochemistry and Structures of $CoC_3H_6^+$: Metallacycle and Metal-Alkene Isomers. *Organometallics* **1994,** *13*, 3480-3490.
39. Kickel, B. L.; Armentrout, P. B., Guided Ion Beam Studies of the Reactions of Group 3 Metal Ions (Sc^+, Y^+, La^+, and Lu^+) with Silane. Electronic State Effects, Comparison to Reactions with Methane, and M^+-SiH_x (x = 0 - 3) Bond Energies. *J. Am. Chem. Soc.* **1995,** *117*, 4057-4070.
40. Beyer, T.; Swinehart, D., Number of multiply-restricted partitions. ASSOC COMPUTING MACHINERY 2 PENN PLAZA, STE 701, NEW YORK, NY 10121-0701 USA: 1973; Vol. 16, pp 379-379.
41. Dalleska, N.; Honma, K.; Sunderlin, L.; Armentrout, P., Solvation of transition metal ions by water. Sequential binding energies of M+ (H2O) x (x= 1-4) for M= Ti to Cu determined by collision-induced dissociation. *Journal of the American Chemical Society* **1994,** *116* (8), 3519-3528.
42. Cox, R. M.; Armentrout, P. B.; de Jong, W. A., Reactions of $Th^+ + H_2$, D_2, and HD Studied by Guided Ion Beam Tandem Mass Spectrometry and Quantum Chemical Calculations. *J. Phys. Chem. B* **2016,** *120*, 1601-1614.
43. Zhang, W.-J.; Demireva, M.; Kim, J.; de Jong, W. A.; Armentrout, P. B., Reactions of U^+ with H_2, D_2, and HD Studied by Guided Ion Beam Tandem Mass Spectrometry and Theory. *J. Phys. Chem. A* **2021,** *125* (36), 7825-7839.
44. Cox, R. M.; Citir, M.; Armentrout, P. B.; Battey, S. R.; Peterson, K. A., Bond Energies of ThO^+ and ThC^+: A Guided Ion Beam and Quantum Chemical Investigation of the Reactions of Thorium Cation with O_2 and CO. *J. Chem. Phys.* **2016,** *144*, 184309.

45. Zhang, W.; Hunt, A. R. E.; Demireva, M.; Kim, J.; Peterson, K. A.; Armentrout, P. B., Bond Energies of UO^+ and UC^+: Guided Ion Beam and Quantum Chemical Studies of the Reactions of Uranium Cation with O_2 and CO. *Isr. J. Chem.* **2023**, e202300026.
46. Armentrout, P.; Sievers, M., Activation of CH4 by Gas-Phase Zr+ and the Thermochemistry of Zr−Ligand Complexes. *The Journal of Physical Chemistry A* **2003,** *107* (22), 4396-4406.
47. Parke, L. G.; Hinton, C. S.; Armentrout, P., Why is hafnium so unreactive?: Experimental and theoretical studies of the reaction of Hf+ with methane. *International Journal of Mass Spectrometry* **2006,** *254* (3), 168-182.
48. Cox, R. M. B., A. R.; Melby, K. M.; French, A. D.; Rodriguez, M. J.; Prange, M. P.; Govind, N.; Peterson, K. A.; Armentrout, P. B., The Reactions of An+ (An+ = Th+, U+ - Am+) + NO Reactions Observed by Inductively Coupled Plasma Tandem Mass Spectrometry *In Progress* **2024**.
49. Bubas, A. R.; Owen, C. J.; Armentrout, P. B., Reactions of Atomic Thorium and Uranium Cations with CF_4 Studied by Guided Ion Beam Tandem Mass Spectrometry. *Int. J. Mass Spectrom.* **2022,** *472*, 116778.

Table 1. Fitting parameters of equation 10.

Reaction	An^+	n	σ	E_0 (eV)
$An^+ + CD_4 \rightarrow AnD^+ + CD_3$	Th^+	2.5 ± 0.30	0.90 ± 0.09	1.62 ± 0.81
	Pa^+	2.5 ± 0.3	1.04 ± 0.10	1.63 ± 0.54
	U^+	2.5 ± 0.3	0.94 ± 0.09	1.76 ± 0.71
	Np^+	2.5 ± 0.3	1.01 ± 0.10	1.70 ± 0.51
	Pu^+	2.5 ± 0.3	1.03 ± 0.10	3.31 ± 0.83
	Am^+	2.5 ± 0.3	1.04 ± 0.10	3.65 ± 0.74
$An^+ + CD_4 \rightarrow AnCD_2^+ + D_2$	Th^+	2.1 ± 0.2	1.30 ± 0.13	0.43 ± 0.78
	Pa^+	2.3 ± 0.2	1.33 ± 0.13	0.59 ± 0.53
	U^+	2.3 ± 0.2	0.87 ± 0.09	0.97 ± 0.68
	Np^+	1.8 ± 0.2	0.98 ± 0.10	0.96 ± 0.47
	Pu^+	2.3 ± 0.2	0.02 ± 0.01	1.39 ± 0.77
$An^+ + CD_4 \rightarrow AnCD_3^+ + D$	Th^+	2.5 ± 0.3	0.12 ± 0.01	1.19 ± 0.80
	Pa^+	2.5 ± 0.3	0.17 ± 0.02	1.86 ± 0.52
	U^+	2.2 ± 0.2	0.08 ± 0.01	1.34 ± 0.68
	Np^+	2.5 ± 0.3	0.05 ± 0.01	1.06 ± 0.50

$An^+ + CD_4 \rightarrow AnCD^+ + D_2 + D$	Th^+	2.5 ± 0.3	0.33 ± 0.03	2.51 ± 0.80
	Pa^+	2.5 ± 0.3	0.23 ± 0.02	2.38 ± 0.52
	U^+	2.5 ± 0.3	0.11 ± 0.01	3.13 ± 0.70
	Np^+	2.5 ± 0.3	0.06 ± 0.01	3.59 ± 0.50
$An^+ + CD_4 \rightarrow AnC^+ + 2D_2$	Th^+	2.5 ± 0.3	0.02 ± 0.01	2.35 ± 0.80
	Pa^+	2.5 ± 0.3	0.10 ± 0.01	2.91 ± 0.52
	U^+	2.5 ± 0.3	0.07 ± 0.01	3.46 ± 0.70

Table 2. Derived bond dissociation energies of An^+–D, An^+–CD_2, An^+–CD_3, An^+–CD, and An^+–C species.

	$D_0(An^+–D)$ (eV)		$D_0(An^+–CD_2)$ (eV)		$D_0(An^+–CD_3)$ (eV)		$D_0(An^+–CD)$ (eV)		$D_0(An^+–C)$ (eV)	
	This work	Literature[a]	This work	Literature[b]	This work	Literature[b]	This work	Literature[b]	This work	Literature
Th^+	2.96 ± 0.81	2.45 ± 0.07	≥ 4.39 ± 0.78	≥ 4.54 ± 0.09	3.39 ± 0.80	2.60 ± 0.30	6.74 ± 0.80	6.27 ± 0.06	5.85 ± 0.80	4.82 ± 0.29[c]
Pa^+	2.94 ± 0.54	*2.35*	4.23 ± 0.53		2.72 ± 0.52		6.87 ± 0.52		5.29 ± 0.52	
U^+	2.82 ± 0.71	2.48 ± 0.06[d]	3.84 ± 0.68	4.17 ± 0.06[e]	3.23 ± 0.68	2.46 ± 0.15[e]	6.12 ± 0.70	5.02 ± 0.10[e]	4.74 ± 0.70	4.03 ± 0.13[f]
Np^+	2.87 ± 0.51	*2.45*	3.86 ± 0.47		3.52 ± 0.50		5.66 ± 0.50			
Pu^+	1.27 ± 0.83	*1.37*	3.43 ± 0.77							
Am^+	0.92 ± 0.74	*0.69*								

a. Ref.[42]unless noted otherwise. Values without uncertainty are an estimate. b. Ref.[23] The reported values have been averaged over results from CH_4 and CD_4. c. Ref.[44]. d. Ref.[43] e. Unpublished results from Armentrout, f. Ref.[45]

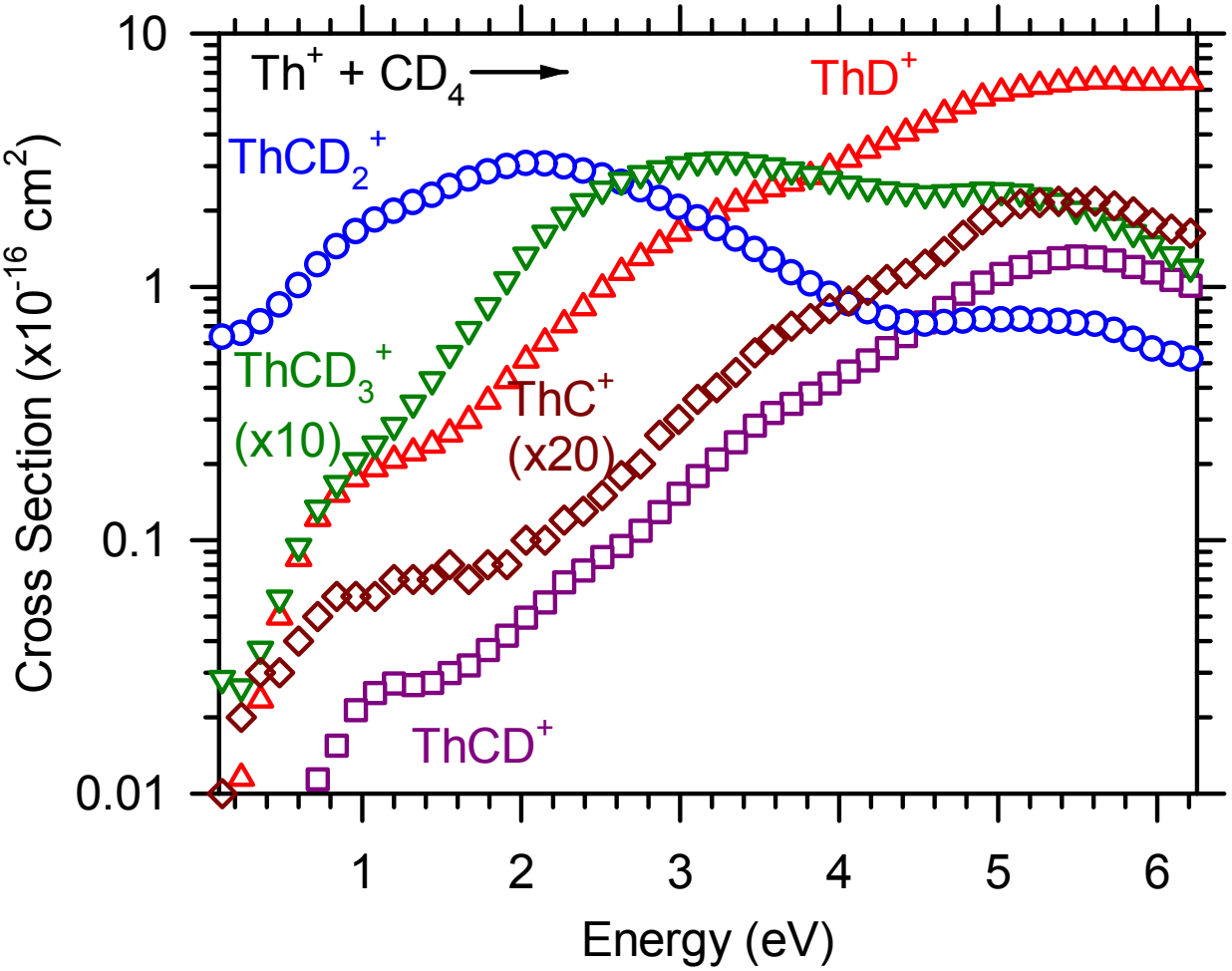

Figure 1. Product ion cross sections as a function of Th^+ kinetic energy in the center-of-mass frame for the reaction $Th^+ + CD_4$. The $ThCD_3^+$ and ThC^+ cross sections are scaled by factors of 10 and 20, respectively, to show the kinetic energy dependences of these product channels more clearly.

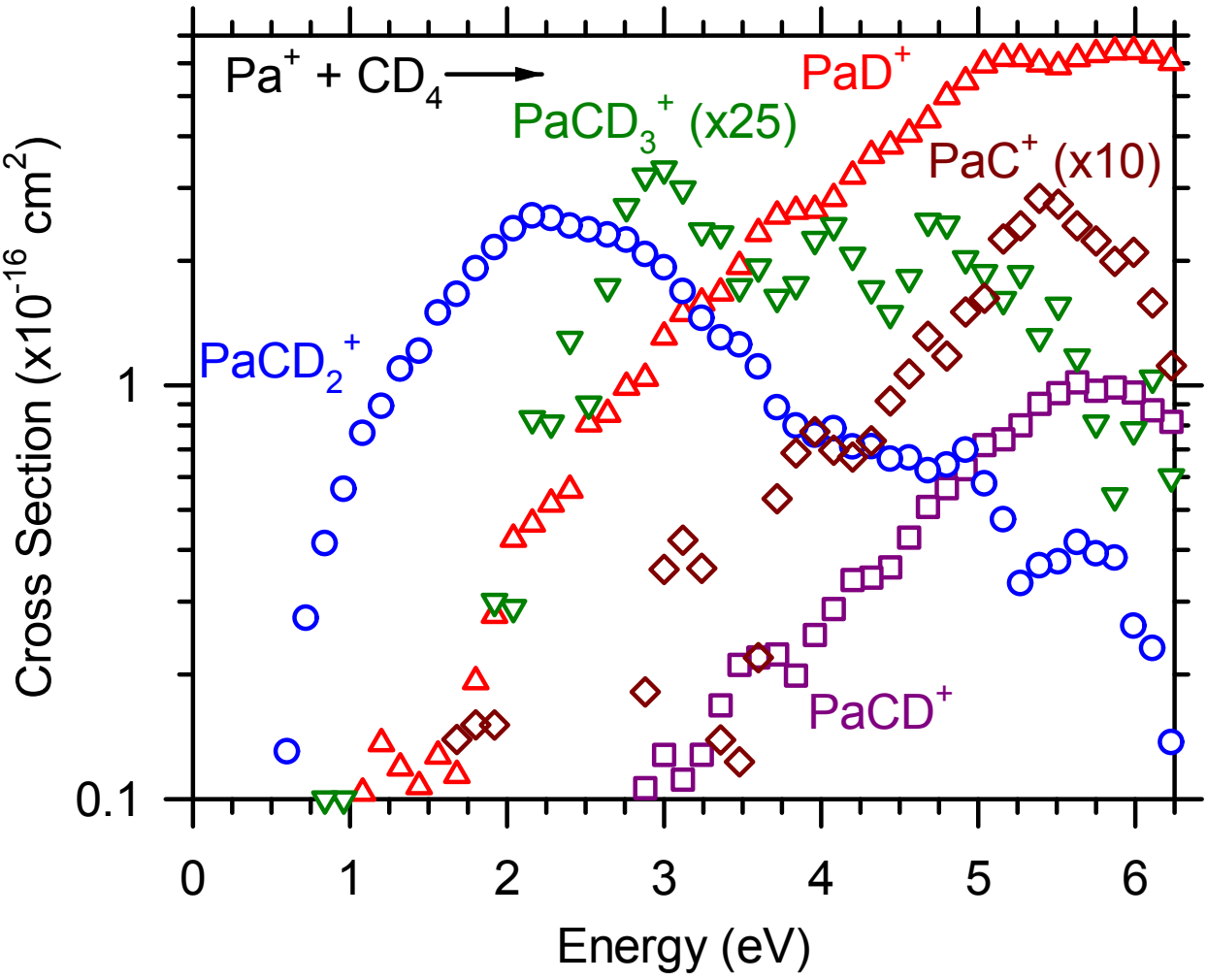

Figure 2. Product ion cross sections as a function of Pa^+ kinetic energy in the center-of-mass frame for the reaction $Pa^+ + CD_4$. The $PaCD_3^+$ and PaC^+ cross sections are scaled by factors of 25 and 10, respectively, to show the kinetic energy dependences of these product channels more clearly.

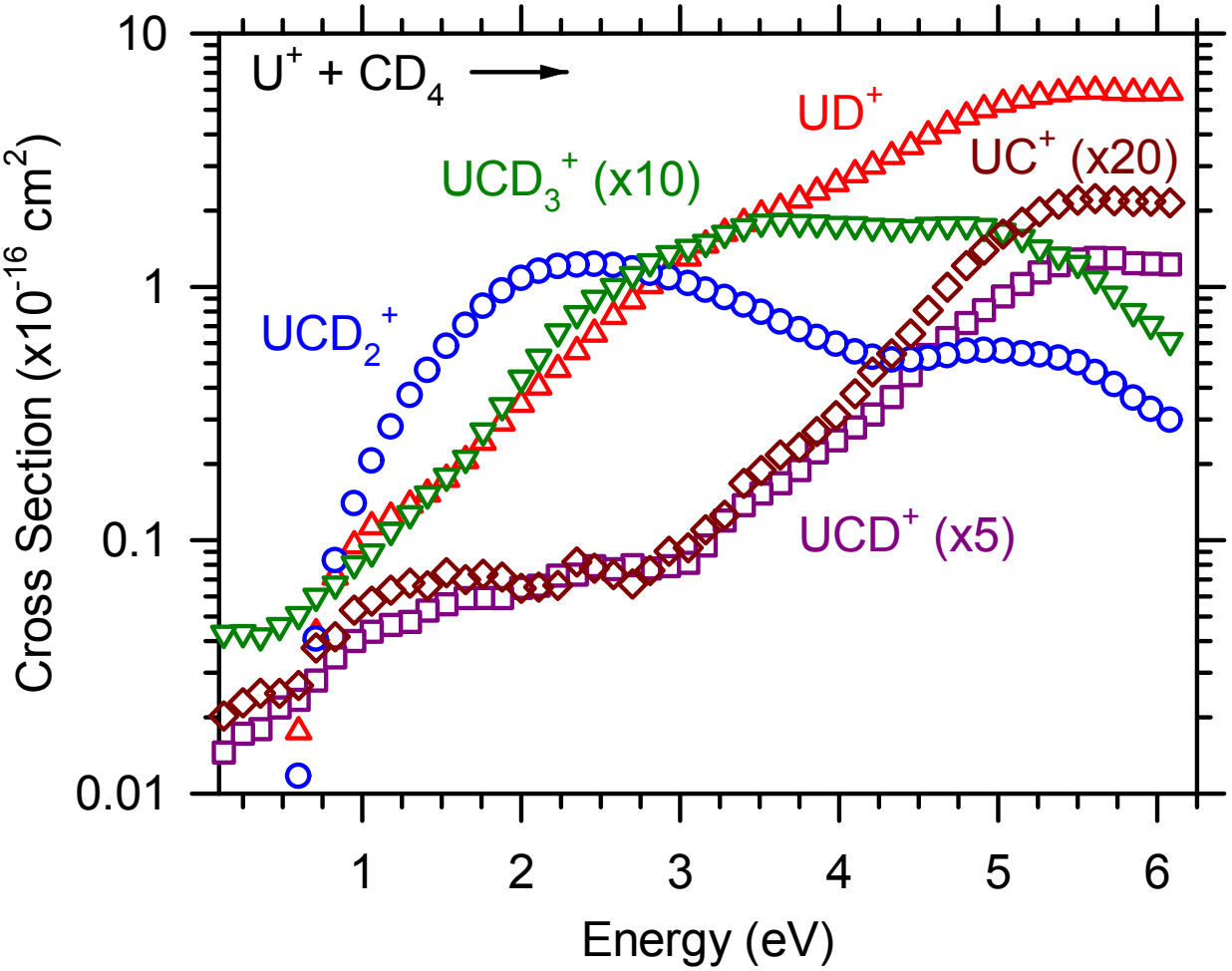

Figure 3. Product ion cross sections as a function of U^+ kinetic energy in the center-of-mass frame for the reaction $U^+ + CD_4$. The UCD_3^+, UCD^+, and UC^+ cross sections are scaled by factors of 10, 5, and 20, respectively, to show the kinetic energy dependences of these product channels more clearly.

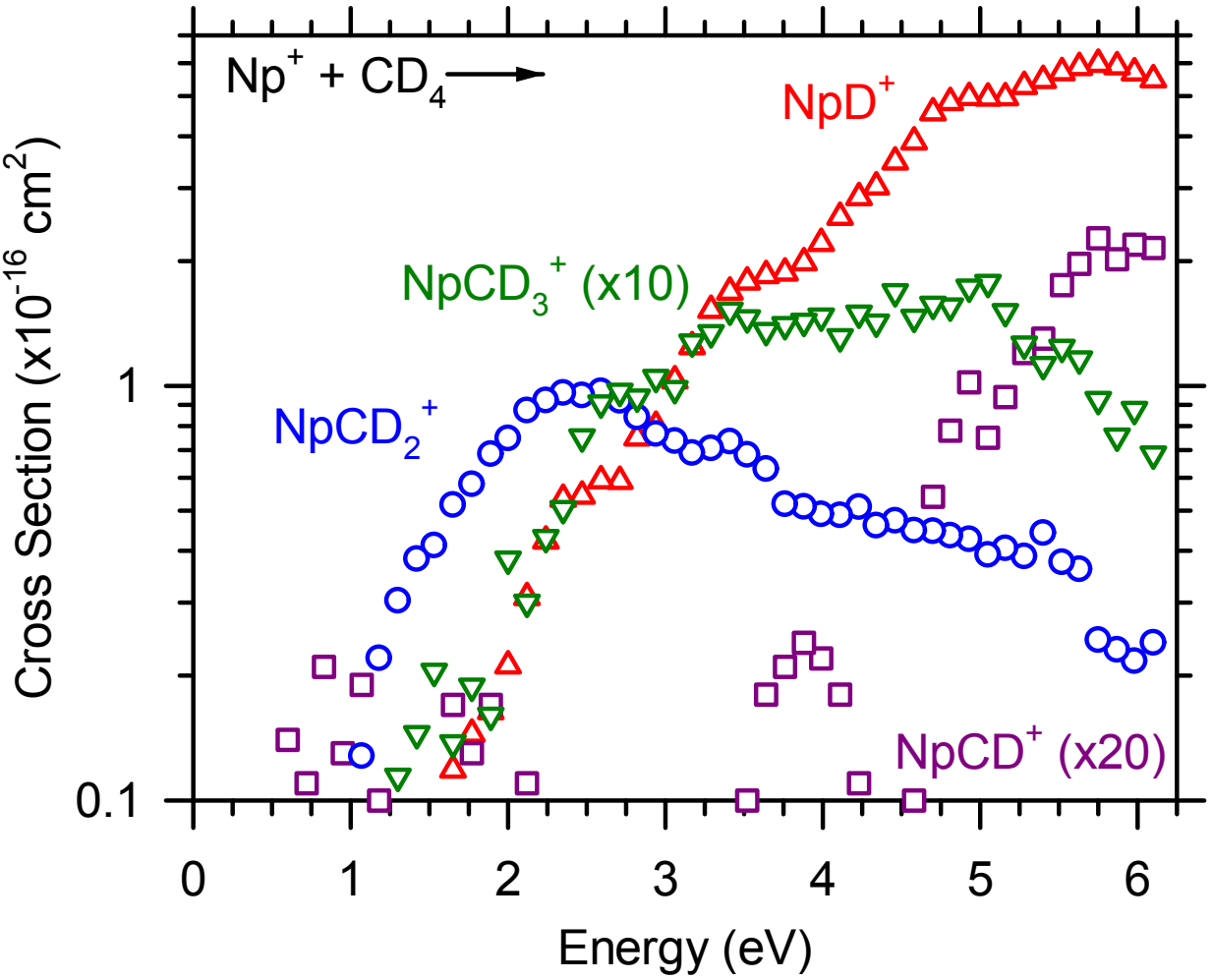

Figure 4. Product ion cross sections as a function of Np^+ kinetic energy in the center-of-mass frame for the reaction $Np^+ + CD_4$. The $NpCD_3^+$ and $NpCD^+$ cross sections are scaled by factors of 10 and 20, respectively, to show the kinetic energy dependences of these product channels more clearly.

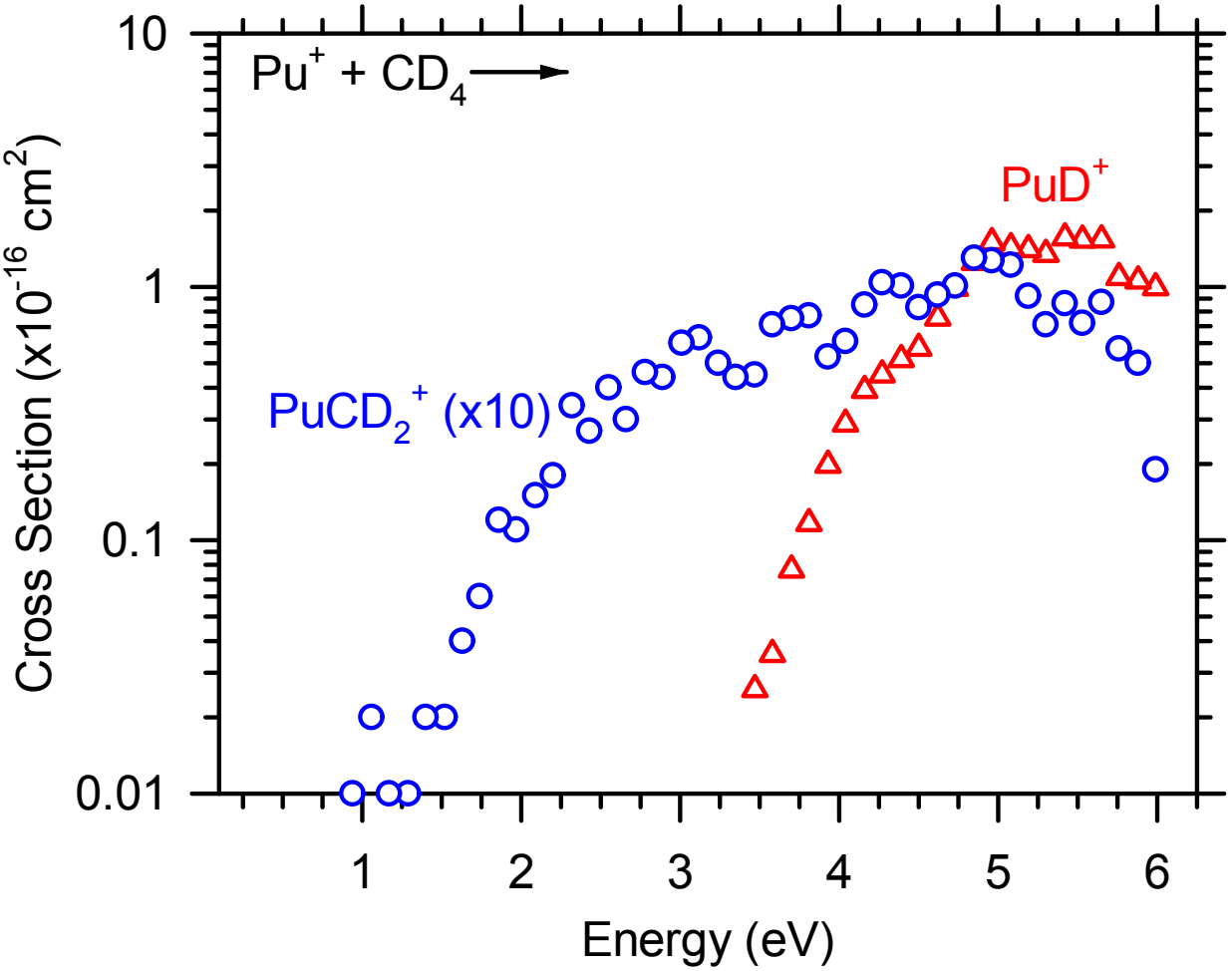

Figure 5. Product ion cross sections as a function of Pu^+ kinetic energy in the center-of-mass frame for the reaction $Pu^+ + CD_4$. The $PuCD_2^+$ cross section is scaled by a factor of 10 to show the kinetic energy dependence of this product channel more clearly.

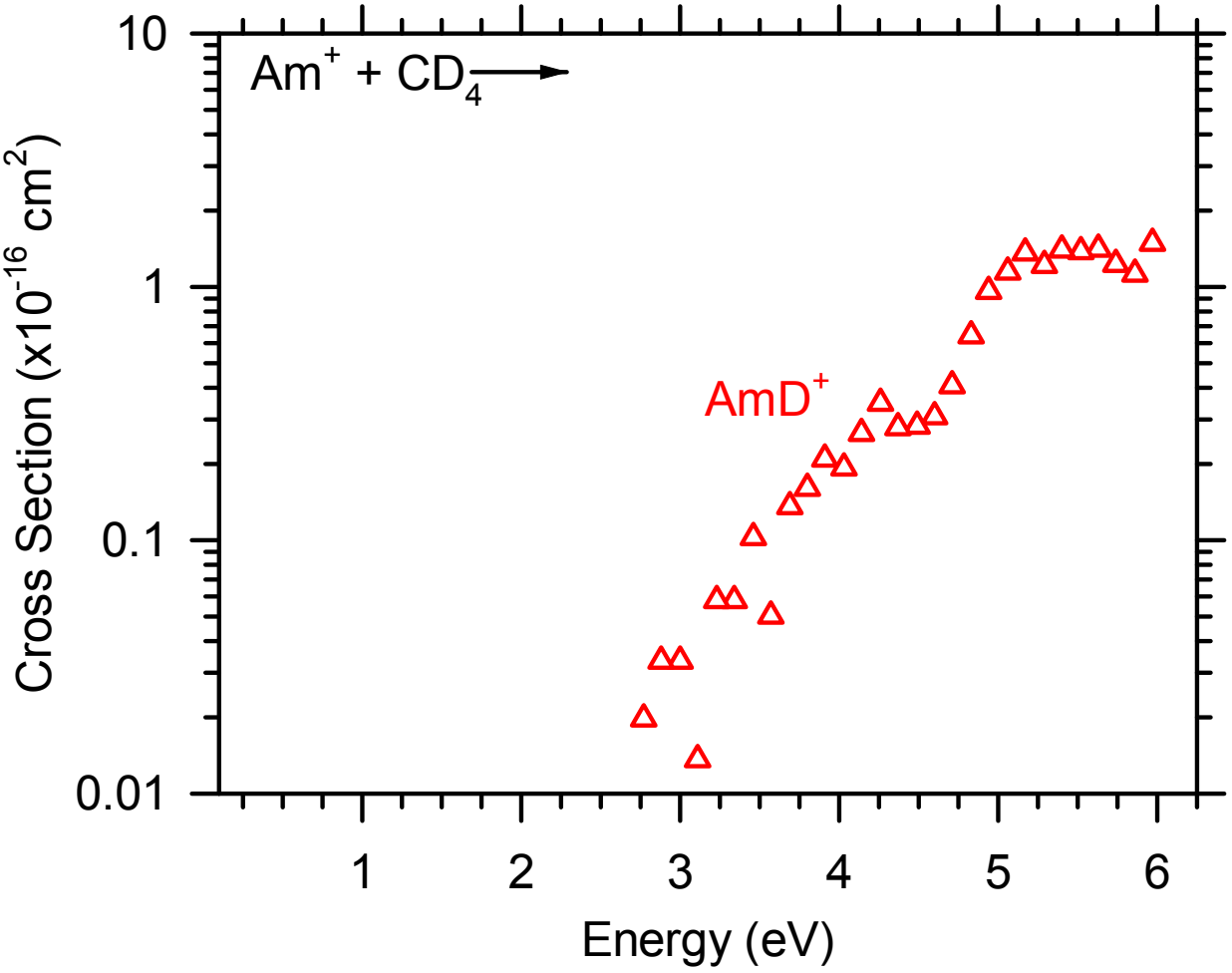

Figure 6. Product ion cross section as a function of Am^+ kinetic energy in the center-of-mass frame for the reaction $Am^+ + CD_4 \rightarrow AmD^+ + CD_3$.

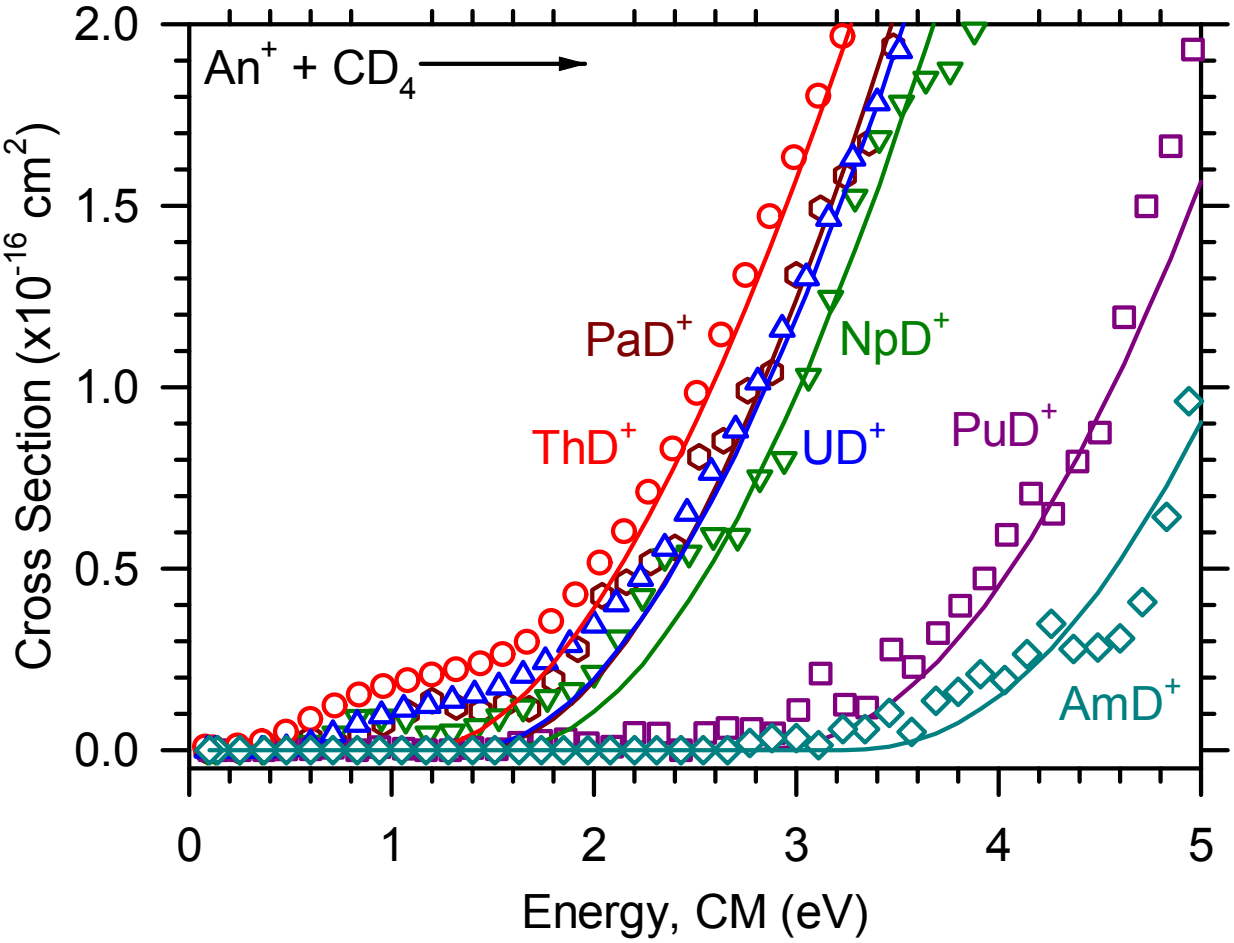

Figure 7. Comparison of the product ion cross sections as a function of An^+ kinetic energy in the center-of-mass frame for the reaction $An^+ + CD_4 \rightarrow AnD^+ + CD_3$. Models using equation 10 to obtain threshold energies, E_0, are shown by the solid lines. $E_0(ThD^+) = 1.62 \pm 0.81$. $E_0(PaD^+) = 1.63 \pm 0.54$. $E_0(UD^+) = 1.76 \pm 0.71$. $E_0(NpD^+) = 1.70 \pm 0.51$. $E_0(PuD^+) = 3.31 \pm 0.83$. $E_0(AmD^+) = 3.65 \pm 0.74$.

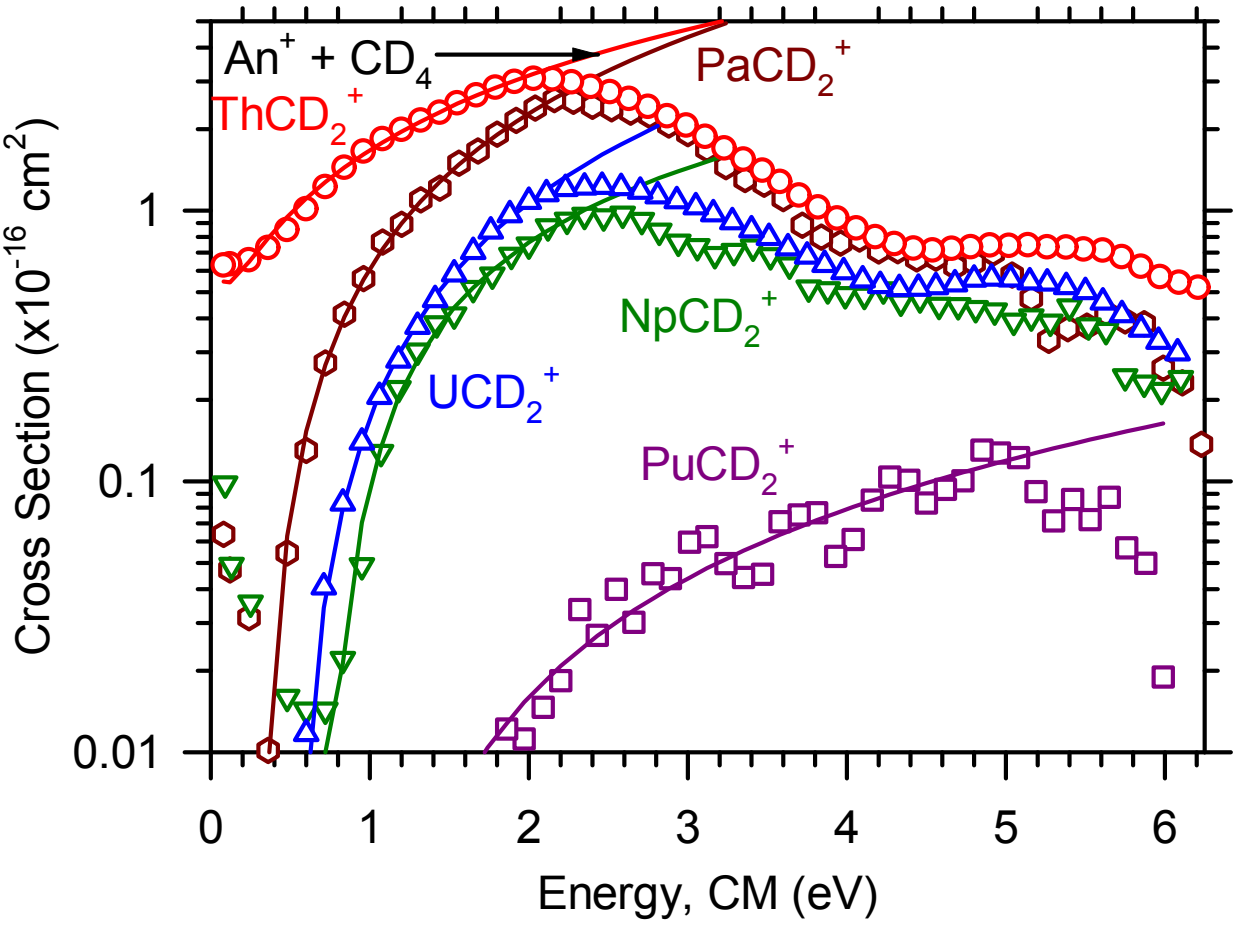

Figure 8. Comparison of product ion cross sections as a function of An^+ kinetic energy in the center-of-mass frame for the reaction $An^+ + CD_4 \rightarrow AnCD_2^+ + D_2$. The $AmCD_2^+$ product was not observed. Models using equation 10 to obtain threshold energies, E_0, are shown by the solid lines. $E_0(ThCD_2^+) = 0.43 \pm 0.78$. $E_0(PaCD_2^+) = 0.59 \pm 0.53$. $E_0(UCD_2^+) = 0.97 \pm 0.68$. $E_0(NpCD_2^+) = 0.96 \pm 0.47$. $E_0(PuCD_2^+) = 1.39 \pm 0.77$.

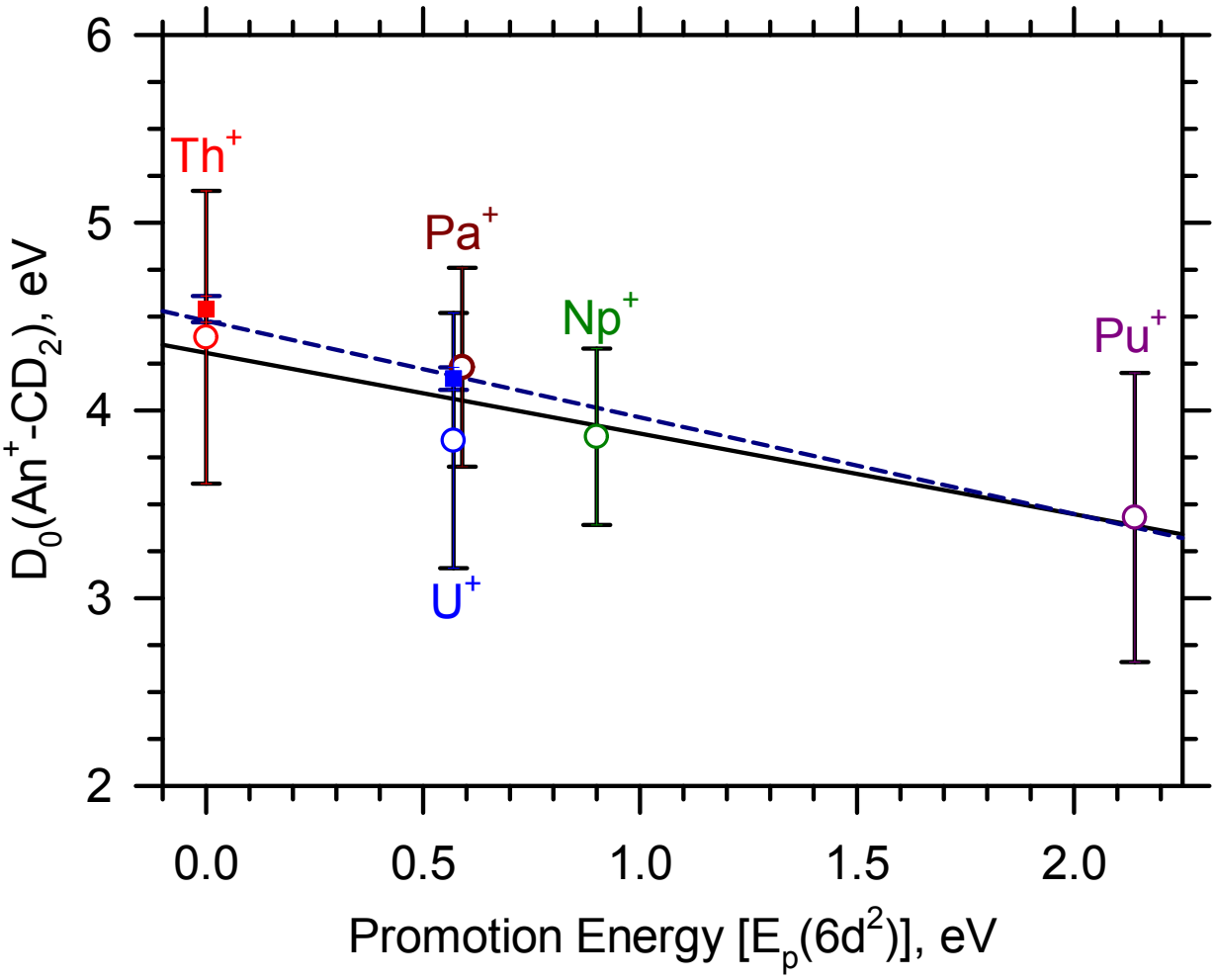

Figure 9. Correlation of $An^+–CD_2$ BDEs with promotion energies of An^+ to a $6d^2$ electronic configuration. Open circles correspond to BDEs from ICP-MS/MS, and filled squares correspond to BDEs from GIBMS studies of the reactions of Th^{+23} and U^+ (unpublished results from Armentrout) with CD_4. The solid black line is the least squares linear regression line using only the BDEs from the present ICP-MS/MS work ($r^2 = 0.84$), and the dashed blue line is the least squares linear regression line using the BDEs from GIBMS for Th and U and the BDEs from the present ICP-MS/MS work for Pa, Np, and Pu ($r^2 = 0.95$). Models of the cross section using equation 10 provide threshold energies used to derive $D_0(An^+–CD_2)$. The $Th^+–CD_2$ BDE is a lower limit to the BDE. For simplicity of the graphic, a directional arrow indicating this BDE as a lower limit has been omitted.

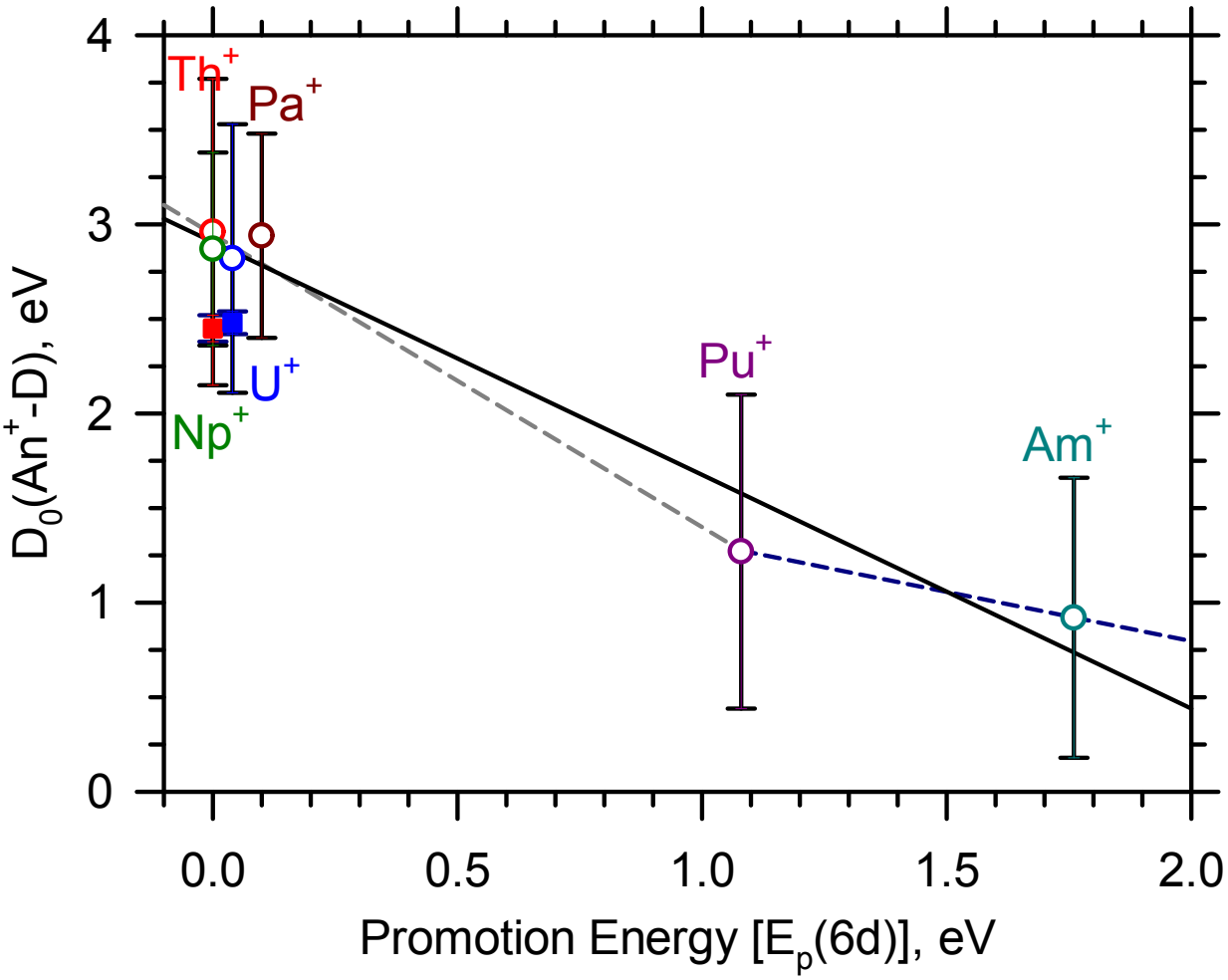

Figure 10. Correlation of An^+–D BDEs with promotion energies of An^+ to a 6d electronic configuration. Open circles correspond to BDEs from ICP-MS/MS, and filled squares correspond to BDEs from GIBMS studies of the reactions of Th^{+42} and U^{+43} with D_2. The solid black line is the least squares linear regression line for Th – Am ($r^2 = 0.96$), the dashed gray line is the least squares linear regression for Th – Pu ($r^2 = 0.98$), and the dashed blue line is the least squares linear regression for Pu and Am. Models of the cross section using equation 10 provide threshold energies used to derive $D_0(An^+–D)$.

Data Availability Statement

The primary data used to support the claims in this paper are included in the primary manuscript or associated Supporting Information section.

Figures 1 – 6 contain the reported absolute reaction cross sections observed in this work.

Figures 7 – 8 Provide the models.

Figures 9 – 10 Are derived from Figures 7 – 8

Table 1 Contains all fitting parameters to the model in Eq 10

Table 2 Contains all thermodynamic values derived from Eq 10

All other data is publicly available through the associated citations with two exceptions. Table 2 reports values from unpublished work from Prof. P. B. Armentrout. This was graciously provided to us with the understanding that it would be published. We will gladly update the citation if/when possible during the review/publication process. We also reference some of our own work that has not yet been submitted for publication. This will be submitted soon and the citation updated when possible.